

# Thermochemical Non-Equilibrium Reentry Flows in Two-Dimensions – Part II

EDISSON SÁVIO DE GÓES MACIEL<sup>(1)</sup> and AMILCAR PORTO PIMENTA<sup>(2)</sup>

IEA – Aeronautical Engineering Division

ITA – Aeronautical Technological Institute

Praça Mal. do Ar Eduardo Gomes,

50 – Vila das Acácias – São José dos Campos – SP – 12228-900

BRAZIL

<sup>(1)</sup>[edisavio@edissonsavio.eng.br](mailto:edisavio@edissonsavio.eng.br) <sup>(1)</sup><http://www.edissonsavio.eng.br> and <sup>(2)</sup>[amilcar@ita.br](mailto:amilcar@ita.br)

*Abstract:* - This work presents a numerical tool implemented to simulate inviscid and viscous flows employing the reactive gas formulation of thermochemical non-equilibrium. The Euler and Navier-Stokes equations, employing a finite volume formulation, on the context of structured and unstructured spatial discretizations, are solved. These variants allow an effective comparison between the two types of spatial discretization aiming verify their potentialities: solution quality, convergence speed, computational cost, etc. The aerospace problems of the hypersonic flow around a double ellipse and around a reentry capsule, in two-dimensions, are simulated. The reactive simulations will involve an air chemical model of five species: N, O, N<sub>2</sub>, O<sub>2</sub> and NO. Seventeen chemical reactions, involving dissociation and recombination, will be studied. The Arrhenius formula will be employed to determine the reaction rates and the law of mass action will be used to determine the source terms of each gas species equation.

*Key-Words:* - Euler and Navier-Stokes equations, Reactive formulation, Thermochemical non-equilibrium, Hypersonic flow, Van Leer algorithm, Finite Volumes, Unstructured discretization.

## 1 Introduction

The study of hypersonic flows has gained momentum with the advent of concepts like the National AeroSpace Plane (NASP) and similar transatmospheric vehicles. Under the very high velocity and temperature conditions experienced by hypersonic vehicles, departure from chemical and thermal equilibrium occurs. Properties of air change dramatically as new chemical species are produced at the expense of others. The simple one temperature model used to describe the energy of air becomes inapplicable, and it becomes necessary to consider one or more additional temperatures (corresponding to vibrational and electronic energies). Determination of aerothermal loads on blunt bodies in such an environment is of great importance.

In high speed flows, any adjustment of chemical composition or thermodynamic equilibrium to a change in local environment requires certain time. This is because the redistribution of chemical species and internal energies require certain number of molecular collisions, and hence a certain characteristic time. Chemical non-equilibrium occurs when the characteristic time for the chemical reactions to reach local equilibrium is of the same order as the characteristic time of the fluid flow.

Similarly, thermal non-equilibrium occurs when the characteristic time for translation and various internal energy modes to reach local equilibrium is of the same order as the characteristic time of the fluid flow. Since chemical and thermal changes are the results of collisions between the constituent particles, non-equilibrium effects prevail in high-speed flows in low-density air.

In chemical non-equilibrium flows the mass conservation equation is applied to each of the constituent species in the gas mixture. Therefore, the overall mass conservation equation is replaced by as many species conservation equations as the number of chemical species considered. The assumption of thermal non-equilibrium introduces additional energy conservation equations – one for every additional energy mode. Thus, the number of governing equations for non-equilibrium flow is much bigger compared to those for perfect gas flow. A complete set of governing equations for non-equilibrium flow may be found in [1-2].

Analysis of non-equilibrium flow is rather complex because (1) the number of equations to be solved is much larger than the Navier-Stokes equations, and (2) there are additional terms like the species production, mass diffusion, and vibrational energy relaxation, etc., that appear in the governing equations. In a typical flight of the NASP flying at

Mach 15, ionization is not expected to occur, and a 5-species air is adequate for the analysis (see [3]). Since the rotational characteristic temperatures for the constituent species (namely N, O, N<sub>2</sub>, O<sub>2</sub>, and NO) are small, the translational and rotational energy modes are assumed to be in equilibrium, whereas the vibrational energy mode is assumed to be in non-equilibrium. [4] has simplified the thermodynamic model by assuming a harmonic oscillator to describe the vibrational energy. Ionic species and electrons are not considered. This simplifies the set of governing equations by eliminating the equation governing electron and electronic excitation energy. [4] has taken the complete set of governing equations from [1], and simplified them for a five-species two-temperature air model.

The problems of chemical non-equilibrium in the shock layers over vehicles flying at high speeds and high altitudes in the Earth's atmosphere have been discussed by several investigators ([5-8]). Most of the existing computer codes for calculating the non-equilibrium reacting flow use the one-temperature model, which assumes that all of the internal energy modes of the gaseous species are in equilibrium with the translational mode ([7-8]). It has been pointed out that such a one-temperature description of the flow leads to a substantial overestimation of the rate of equilibrium because of the elevated vibrational temperature ([6]). A three-temperature chemical-kinetic model has been proposed by [2] to describe the relaxation phenomena correctly in such a flight regime. However, the model is quite complex and requires many chemical rate parameters which are not yet known. As a compromise between the three-temperature and the conventional one-temperature model, a two-temperature chemical-kinetic model has been developed ([5-6]), which is designated herein as the TT<sub>v</sub> model. The TT<sub>v</sub> model uses one temperature T to characterize both the translational energy of the atoms and molecules and the rotational energy of the molecules, and another temperature T<sub>v</sub> to characterize the vibrational energy of the molecules, translational energy of the electrons, and electronic excitation energy of atoms and molecules. The model has been applied to compute the thermodynamic properties behind a normal shock wave in a flow through a constant-area duct ([9-10]). Radiation emission from the non-equilibrium flow has been calculated using the Non-equilibrium Air Radiation (NEQAIR) program ([11-12]). The flow and the radiation computations have been packaged into a single computer program, the Shock-Tube Radiation Program (STRAP) ([10]).

A first-step assessment of the TT<sub>v</sub> model was made in [10] where it was used in computing the flow properties and radiation emission from the flow in a shock tube for pure nitrogen undergoing dissociation and weak ionization (ionization fraction less than 0.1%). Generally good agreement was found between the calculated radiation emission and those obtained experimentally in shock tubes ([13-15]). The only exception involved the vibrational temperature. The theoretical treatment of the vibrational temperature could not be validated because the existing data on the vibrational temperature behind a normal shock wave ([15]) are those for an electronically excited state of the molecular nitrogen ion N<sub>2</sub><sup>+</sup> instead of the ground electronic state of the neutral nitrogen molecule N<sub>2</sub> which is calculated in the theoretical model. The measured vibrational temperature of N<sub>2</sub><sup>+</sup> was much smaller than the calculated vibrational temperature for N<sub>2</sub>.

This work, second of this study, describes a numerical tool to perform thermochemical non-equilibrium simulations of reactive flow in two-dimensions. The [16] scheme, in its first- and second-order versions, is implemented to accomplish the numerical simulations. The Euler and Navier-Stokes equations, on a finite volume context and employing structured and unstructured spatial discretizations, are applied to solve the "hot gas" hypersonic flows around a double ellipse and around a reentry capsule in two-dimensions. The second-order version of the [16] scheme is obtained from a "MUSCL" extrapolation procedure (details in [17] and [35]) in a context of structured spatial discretization. In the unstructured context, only first-order solutions are obtained. The convergence process is accelerated to the steady state condition through a spatially variable time step procedure, which has proved effective gains in terms of computational acceleration (see [18-19]).

The reactive simulations involve an air chemical model of five species: N, O, N<sub>2</sub>, O<sub>2</sub>, and NO. Seventeen chemical reactions, involving dissociation and recombination, are simulated by the proposed model. The Arrhenius formula is employed to determine the reaction rates and the law of mass action is used to determine the source terms of each gas specie equation.

The results have demonstrated that the most correct aerodynamic coefficient of lift in the reentry capsule problem is obtained by the [16] scheme with first-order accuracy, in a viscous formulation, to a reactive condition of thermochemical non-equilibrium. In the double ellipse problem, the most

severe lift coefficient in the thermochemical non-equilibrium formulation is due to the [16] scheme, first-order accurate, in an inviscid condition. Taking into account both problems, the reentry capsule problem presents the most severe drag coefficients. The lift coefficient is better estimated in the thermochemical non-equilibrium formulation than in the thermal equilibrium and chemical non-equilibrium formulation. Considering thermochemical non-equilibrium, the cheapest algorithm was due to [16], inviscid, first-order accurate, unstructured. Moreover, the shock position is closer to the geometry as using the reactive formulations than the ideal gas formulation. It was verified in the inviscid and viscous cases.

## 2 Formulation to Reactive Flow in Thermochemical Non-Equilibrium

### 2.1 Reactive Equations in Two-Dimensions

The reactive Navier-Stokes equations in thermal and chemical non-equilibrium were implemented on a finite volume context, in the two-dimensional space. In this case, these equations in integral and conservative forms can be expressed by:

$$\frac{\partial}{\partial t} \int_V Q dV + \int_S \vec{F} \cdot \vec{n} dS = \int_V S_{CV} dV, \text{ with}$$

$$\vec{F} = (E_e - E_v) \vec{i} + (F_e - F_v) \vec{j}, \quad (1)$$

where: Q is the vector of conserved variables, V is the volume of a computational cell,  $\vec{F}$  is the complete flux vector,  $\vec{n}$  is the unit vector normal to the flux face, S is the flux area,  $S_{CV}$  is the chemical and vibrational source term,  $E_e$  and  $F_e$  are the convective flux vectors or the Euler flux vectors in the x and y directions, respectively,  $E_v$  and  $F_v$  are the viscous flux vectors in the x and y directions, respectively. The  $\vec{i}$  and  $\vec{j}$  unit vectors define the Cartesian coordinate system. Nine (9) conservation equations are solved: one of general mass conservation, two of linear momentum conservation, one of total energy, four of species mass conservation and one of the vibrational internal energy of the molecules. Therefore, one of the species is absent of the iterative process. The CFD (“Computational Fluid Dynamics”) literature recommends that the species of biggest mass fraction of the gaseous mixture should be omitted, aiming to result in a minor numerical accumulation

error, corresponding to the biggest mixture constituent (in the case, the air). To the present study, in which is chosen a chemical model to the air composed of five (5) chemical species (N, O, N<sub>2</sub>, O<sub>2</sub> and NO) and seventeen (17) chemical reactions, being fifteen (15) dissociation reactions (endothermic reactions) and two (2) of exchange or recombination, this species can be the N<sub>2</sub> or the O<sub>2</sub>. To this work, it was chosen the N<sub>2</sub>. The vectors Q,  $E_e$ ,  $F_e$ ,  $E_v$ ,  $F_v$  and  $S_{CV}$  can, hence, be defined as follows ([4]):

$$Q = \begin{Bmatrix} \rho \\ \rho u \\ \rho v \\ e \\ \rho_1 \\ \rho_2 \\ \rho_4 \\ \rho_5 \\ \rho e_v \end{Bmatrix}, E_e = \begin{Bmatrix} \rho u \\ \rho u^2 + p \\ \rho uv \\ \rho Hu \\ \rho_1 u \\ \rho_2 u \\ \rho_4 u \\ \rho_5 u \\ \rho e_v u \end{Bmatrix}, F_e = \begin{Bmatrix} \rho v \\ \rho uv \\ \rho v^2 + p \\ \rho Hv \\ \rho_1 v \\ \rho_2 v \\ \rho_4 v \\ \rho_5 v \\ \rho e_v v \end{Bmatrix}; \quad (2)$$

$$E_v = \frac{1}{Re} \begin{Bmatrix} 0 \\ \tau_{xx} \\ \tau_{xy} \\ \tau_{xx} u + \tau_{xy} v - q_{f,x} - q_{v,x} - \phi_x \\ -\rho_1 v_{1x} \\ -\rho_2 v_{2x} \\ -\rho_4 v_{4x} \\ -\rho_5 v_{5x} \\ -q_{v,x} - \phi_{v,x} \end{Bmatrix}; \quad (3)$$

$$F_v = \frac{1}{Re} \begin{Bmatrix} 0 \\ \tau_{xy} \\ \tau_{yy} \\ \tau_{xy} u + \tau_{yy} v - q_{f,y} - q_{v,y} - \phi_y \\ -\rho_1 v_{1y} \\ -\rho_2 v_{2y} \\ -\rho_4 v_{4y} \\ -\rho_5 v_{5y} \\ -q_{v,y} - \phi_{v,y} \end{Bmatrix}, \quad (4)$$

$$S_{CV} = \left\{ \begin{array}{c} 0 \\ 0 \\ 0 \\ 0 \\ \dot{\omega}_1 \\ \dot{\omega}_2 \\ \dot{\omega}_4 \\ \dot{\omega}_5 \\ \sum_{s=\text{mol}} \rho_s (e_{v,s}^* - e_{v,s}) / \tau_s + \sum_{s=\text{mol}} \dot{\omega}_s e_{v,s} \end{array} \right\}, \quad (5)$$

in which:  $\rho$  is the mixture density;  $u$  and  $v$  are Cartesian components of the velocity vector in the  $x$  and  $y$  directions, respectively;  $p$  is the fluid static pressure;  $e$  is the fluid total energy;  $\rho_1, \rho_2, \rho_4$  and  $\rho_5$  are densities of the N, O, O<sub>2</sub> and NO, respectively;  $H$  is the mixture total enthalpy;  $e_v$  is the sum of the vibrational energy of the molecules; the  $\tau$ 's are the components of the viscous stress tensor;  $q_{f,x}$  and  $q_{f,y}$  are the frozen components of the Fourier-heat-flux vector in the  $x$  and  $y$  directions, respectively;  $q_{v,x}$  and  $q_{v,y}$  are the components of the Fourier-heat-flux vector calculated with the vibrational thermal conductivity and vibrational temperature;  $\rho_s v_{sx}$  and  $\rho_s v_{sy}$  represent the species diffusion flux, defined by the Fick law;  $\phi_x$  and  $\phi_y$  are the terms of mixture diffusion;  $\phi_{v,x}$  and  $\phi_{v,y}$  are the terms of molecular diffusion calculated at the vibrational temperature;  $\dot{\omega}_s$  is the chemical source term of each species equation, defined by the law of mass action;  $e_v^*$  is the molecular-vibrational-internal energy calculated with the translational/rotational temperature; and  $\tau_s$  is the translational-vibrational characteristic relaxation time of each molecule.

The viscous stresses, in N/m<sup>2</sup>, are determined, according to a Newtonian fluid model, by:

$$\begin{aligned} \tau_{xx} &= 2\mu \frac{\partial u}{\partial x} - \frac{2}{3}\mu \left( \frac{\partial u}{\partial x} + \frac{\partial v}{\partial y} \right), \\ \tau_{xy} &= \mu \left( \frac{\partial u}{\partial y} + \frac{\partial v}{\partial x} \right) \quad \text{and} \quad \tau_{yy} = 2\mu \frac{\partial v}{\partial y} - \frac{2}{3}\mu \left( \frac{\partial u}{\partial x} + \frac{\partial v}{\partial y} \right), \end{aligned} \quad (6)$$

in which  $\mu$  is the fluid molecular viscosity.

The frozen components of the Fourier-heat-flux vector, which considers only thermal conduction, are defined by:

$$q_{f,x} = -k_f \frac{\partial T}{\partial x} \quad \text{and} \quad q_{f,y} = -k_f \frac{\partial T}{\partial y}, \quad (7)$$

where  $k_f$  is the mixture frozen thermal conductivity, calculated conform presented in [20]. The vibrational components of the Fourier-heat-flux vector are calculated as follows:

$$q_{v,x} = -k_v \frac{\partial T_v}{\partial x} \quad \text{and} \quad q_{v,y} = -k_v \frac{\partial T_v}{\partial y}, \quad (8)$$

in which  $k_v$  is the vibrational thermal conductivity and  $T_v$  is the vibrational temperature, what characterizes this model as of two temperatures: translational/rotational and vibrational. The calculation of  $T_v$  and  $k_v$  is demonstrated in [20].

The terms of species diffusion, defined by the Fick law, to a condition of thermal non-equilibrium, are determined by ([4]):

$$\rho_s v_{sx} = -\rho D_s \frac{\partial Y_{MF,s}}{\partial x} \quad \text{and} \quad \rho_s v_{sy} = -\rho D_s \frac{\partial Y_{MF,s}}{\partial y}, \quad (9)$$

with "s" referent to a given species,  $Y_{MF,s}$  being the molar fraction of the species, defined as:

$$Y_{MF,s} = \frac{\rho_s / M_s}{\sum_{k=1}^{ns} \rho_k / M_k} \quad (10)$$

and  $D_s$  is the species-effective-diffusion coefficient.

The diffusion terms  $\phi_x$  and  $\phi_y$  which appear in the energy equation are defined by ([21]):

$$\phi_x = \sum_{s=1}^{ns} \rho_s v_{sx} h_s \quad \text{and} \quad \phi_y = \sum_{s=1}^{ns} \rho_s v_{sy} h_s, \quad (11)$$

being  $h_s$  the specific enthalpy (sensible) of the chemical species "s". Details of the calculation of the specific enthalpy, see [22-23; 34]. The molecular diffusion terms calculated at the vibrational temperature,  $\phi_{v,x}$  and  $\phi_{v,y}$ , which appear in the vibrational-internal-energy equation are defined by ([4]):

$$\phi_{v,x} = \sum_{s=\text{mol}} \rho_s v_{sx} h_{v,s} \text{ and } \phi_{v,y} = \sum_{s=\text{mol}} \rho_s v_{sy} h_{v,s}, \quad (12)$$

with  $h_{v,s}$  being the specific enthalpy (sensible) of the chemical species “s” calculated at the vibrational temperature  $T_v$ . The sum of Eq. (12), as also those present in Eq. (5), considers only the molecules of the system, namely:  $N_2$ ,  $O_2$  and  $NO$ .

### 2.2 Chemical and vibrational models

The chemical model employed to the case of thermochemical non-equilibrium is the same employed to the case of thermal equilibrium and chemical non-equilibrium (see [22-23; 34]). The unique difference is in the calculation of the species production rates, where a temperature of reaction rate control is introduced in the place of the translational/rotational temperature, which is employed in the calculation of such rates in the thermal equilibrium and chemical non-equilibrium case. This procedure aims a couple between vibration and dissociation. This temperature is defined as:  $T_{\text{rrc}} = \sqrt{T \times T_v}$ , where  $T$  is the translational/rotational temperature and  $T_v$  is the vibrational temperature. This temperature  $T_{\text{rrc}}$  replaces the translational/rotational temperature in the calculation of the species production rates, as proposed by [24]. The vibrational model is described in [20].

### 3 Unstructured [16] Algorithm to Thermochemical Non-Equilibrium

Considering the two-dimensional and unstructured case, the algorithm follows that described in [22, 25, 34], considering, however, the vibrational contribution ([20, 26]) and the version of the two-temperature model to the frozen speed of sound, presented in [26]. Hence, the discrete-dynamic-convective flux is defined by:

$$R_1 = |S|_1 \left\{ \frac{1}{2} M_1 \left[ \begin{pmatrix} \rho a \\ \rho a u \\ \rho a v \\ \rho a H \end{pmatrix}_L + \begin{pmatrix} \rho a \\ \rho a u \\ \rho a v \\ \rho a H \end{pmatrix}_R \right] - \frac{1}{2} \phi_1 \left[ \begin{pmatrix} \rho a \\ \rho a u \\ \rho a v \\ \rho a H \end{pmatrix}_R - \begin{pmatrix} \rho a \\ \rho a u \\ \rho a v \\ \rho a H \end{pmatrix}_L \right] \right\} + \begin{pmatrix} 0 \\ S_x p \\ S_y p \\ 0 \end{pmatrix}_1, \quad (13)$$

the discrete-chemical-convective flux is defined by:

$$R_1 = |S|_1 \left\{ \frac{1}{2} M_1 \left[ \begin{pmatrix} \rho_1 a \\ \rho_2 a \\ \rho_4 a \\ \rho_5 a \end{pmatrix}_L + \begin{pmatrix} \rho_1 a \\ \rho_2 a \\ \rho_4 a \\ \rho_5 a \end{pmatrix}_R \right] - \frac{1}{2} \phi_1 \left[ \begin{pmatrix} \rho_1 a \\ \rho_2 a \\ \rho_4 a \\ \rho_5 a \end{pmatrix}_R - \begin{pmatrix} \rho_1 a \\ \rho_2 a \\ \rho_4 a \\ \rho_5 a \end{pmatrix}_L \right] \right\}, \quad (14)$$

and the discrete-vibrational-convective flux is determined by:

$$R_1 = |S|_1 \left\{ \frac{1}{2} M_1 [(\rho e_{v,a})_L + (\rho e_{v,a})_R] - \frac{1}{2} \phi_1 [(\rho e_{v,a})_R - (\rho e_{v,a})_L] \right\}, \quad (15)$$

where the fluxes are calculated at the interface  $l = 1$ , for example, according to [26] notation. The same definitions presented in [26] are valid to this algorithm. The time integration is performed employing the Runge-Kutta explicit method of five stages, second-order accurate, to the three types of convective flux. To the dynamic part, this method can be represented in general form by:

$$\begin{aligned} Q_i^{(0)} &= Q_i^{(n)} \\ Q_i^{(k)} &= Q_i^{(0)} - \alpha_k \Delta t_i R(Q_i^{(k-1)})/V_i, \\ Q_i^{(n+1)} &= Q_i^{(k)} \end{aligned} \quad (16)$$

to the chemical part, it can be represented in general form by:

$$\begin{aligned} Q_i^{(0)} &= Q_i^{(n)} \\ Q_i^{(k)} &= Q_i^{(0)} - \alpha_k \Delta t_i [R(Q_i^{(k-1)})/V_i - S_C(Q_i^{(k-1)})], \\ Q_i^{(n+1)} &= Q_i^{(k)} \end{aligned} \quad (17)$$

where the chemical source term  $S_C$  is calculated with the temperature  $T_{\text{rrc}}$ . Finally, to the vibrational part:

$$\begin{aligned} Q_i^{(0)} &= Q_i^{(n)} \\ Q_i^{(k)} &= Q_i^{(0)} - \alpha_k \Delta t_i [R(Q_i^{(k-1)})/V_i - S_v(Q_i^{(k-1)})], \\ Q_i^{(n+1)} &= Q_i^{(k)} \end{aligned} \quad (18)$$

in which:

$$S_v = \sum_{s=\text{mol}} q_{T-v,s} + \sum_{s=\text{mol}} S_{C,s} e_{v,s}; \quad (19)$$

with  $k = 1, \dots, 5$ ;  $\alpha_1 = 1/4$ ,  $\alpha_2 = 1/6$ ,  $\alpha_3 = 3/8$ ,  $\alpha_4 = 1/2$  and  $\alpha_5 = 1$ . The [27] heat flux due to translational-

vibrational relaxation,  $q_{T-v,s}$ , is defined in [20, 26]. This scheme is first-order accurate in space and second-order accurate in time. The second-order of spatial accuracy is obtained by the “MUSCL” procedure (details in [17] and [35]).

The viscous formulation follows that of [28], which adopts the Green theorem to calculate primitive variable gradients. The viscous vectors are obtained by arithmetical average between cell (i,j) and its neighbors. As was done with the convective terms, there is a need to separate the viscous flux in three parts: dynamical viscous flux, chemical viscous flux and vibrational chemical flux. The dynamical part corresponds to the first four equations of the Navier-Stokes ones, the chemical part corresponds to the following four equations and the vibrational part corresponds to the last equation.

The spatially variable time step technique has provided excellent convergence gains as demonstrated in [18-19] and is implemented in the codes presented in this work.

## 4 Results

Tests were performed in a Dual-Core Intel processor notebook with 2.3GHz of clock and 2.0GBytes of RAM. As the interest of this work is steady state problems, it is necessary to define a criterion which guarantees the convergence of the numerical results. The criterion adopted was to consider a reduction of no minimal three (3) orders of magnitude in the value of the maximum residual in the calculation domain, a typical CFD community criterion. The residual of each cell was defined as the numerical value obtained from the discretized conservation equations. As there are nine (9) conservation equations to each cell, the maximum value obtained from these equations is defined as the residual of this cell. Hence, this residual is compared with the residual of the other cells, calculated of the same way, to define the maximum residual in the calculation domain. In the simulations, the attack angle was set equal to zero.

### 4.1 Initial Conditions

The initial conditions are presented in Tabs. 1 and 2. The Reynolds number is obtained from data of [29]. The boundary conditions to this problem of reactive flow are detailed in [30], as well the description of the computational configurations.

The first geometry under study is a double ellipse, whereas the second one is a reentry capsule. These configurations are described in Figs 1 and 2 and the computational meshes, to inviscid and viscous cases, are presented in Figs. 3 to 6. The dimensionless

employed in the Euler and Navier-Stokes equations in this study are also described in [30].

**Table 1 Initial conditions to the problem of the double ellipse.**

Property	Value
$M_\infty$	15.0
$\rho_\infty$	0.00922 kg/m <sup>3</sup>
$p_\infty$	794 Pa
$U_\infty$	5,208 m/s
$T_\infty$	300 K
$T_{v,\infty}$	300 K
altitude	50,000 m
$c_N$	10 <sup>-9</sup>
$c_O$	0.07955
$c_{O_2}$	0.13400
$c_{NO}$	0.05090
L	5.0 m
$Re_\infty$	1.574x10 <sup>6</sup>

**Table 2 Initial conditions to the problem of the reentry capsule.**

Property	Value
$M_\infty$	10.6
$\rho_\infty$	0.02863 kg/m <sup>3</sup>
$p_\infty$	3,885 Pa
$U_\infty$	4,628 m/s
$T_\infty$	473 K
$T_{v,\infty}$	473 K
Altitude	40,000 m
$c_N$	10 <sup>-9</sup>
$c_O$	0.07955
$c_{O_2}$	0.13400
$c_{NO}$	0.05090
L	3.0 m
$Re_\infty$	3.468x10 <sup>6</sup>

### 4.2 Description of the Geometrical Configurations and Employed Meshes

Figures 1 and 2 exhibit the geometrical configurations of the geometries under study in this work. In Figure 1 is presented the double ellipse configuration and in Fig. 2 is presented the reentry capsule configuration.

Figures 3 and 4 present the inviscid and viscous double ellipse meshes, whereas Figs. 5 and 6 present the inviscid and viscous reentry capsule meshes. The unstructured meshes are obtained transforming a mesh of quadrilaterals in a mesh of triangles and the connectivity, neighboring, ghost and node

coordinate tables are generated in a pre-processing stage of the computation.

nodes in the structured case and of 6,272 triangular cells and 3,250 nodes in the unstructured case.

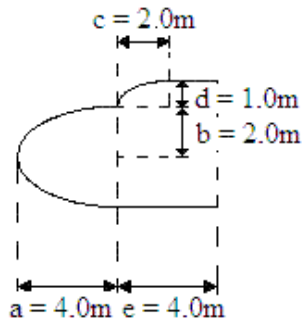


Figure 1. Double ellipse configuration.

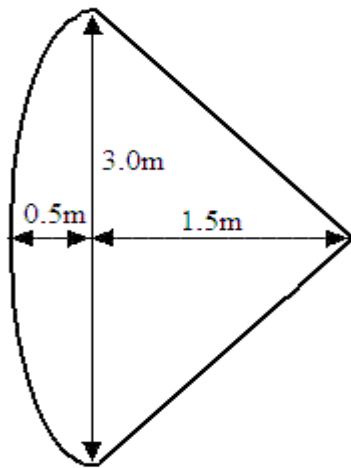


Figure 2. Reentry capsule configuration.

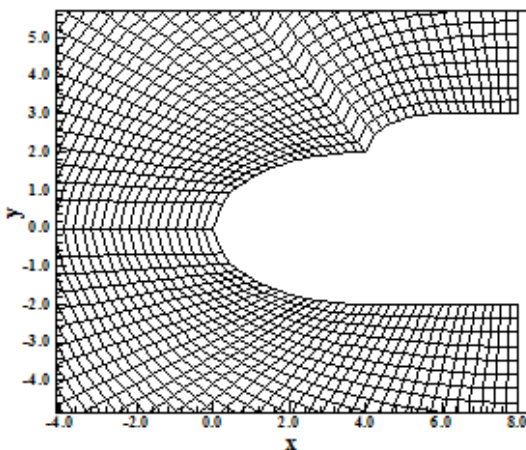


Figure 3. Double ellipse mesh (Inviscid case).

The double ellipse mesh is composed of 3,528 rectangular cells and 3,650 nodes in the structured case and of 7,056 triangular cells and 3,650 nodes in the unstructured case. The reentry capsule is composed of 3,136 rectangular cells and 3,250

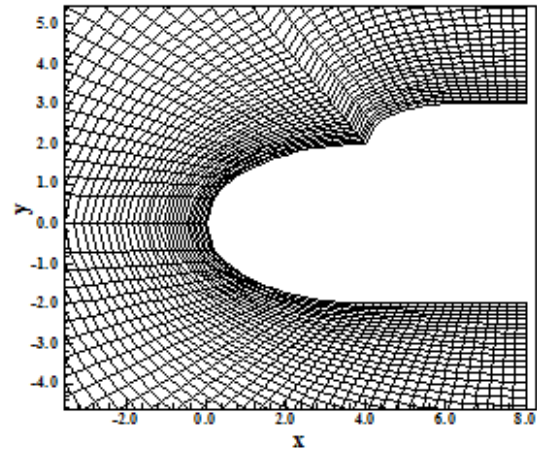


Figure 4. Double ellipse mesh (Viscous case).

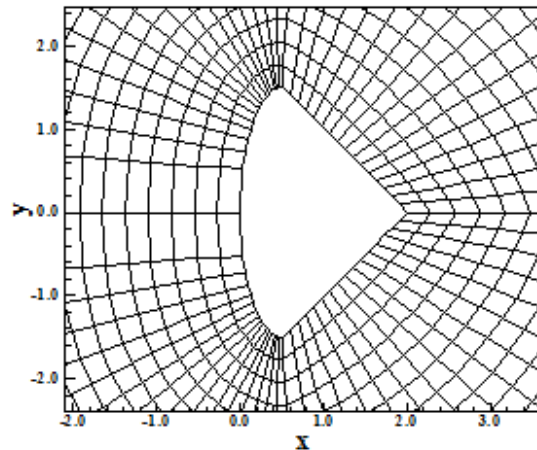


Figure 5. Reentry capsule mesh (Inviscid case).

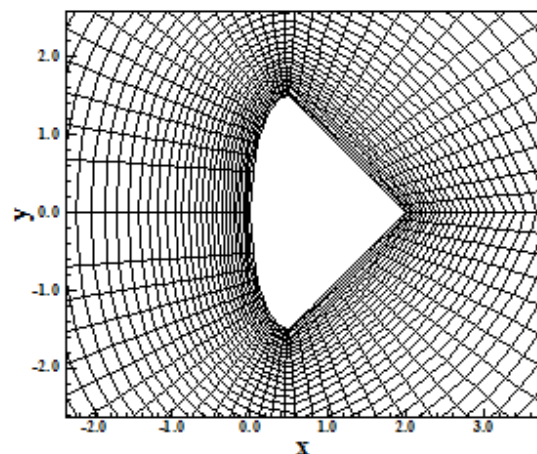


Figure 6. Reentry capsule mesh (Viscous case).

### 4.3 Studied Cases

Table 3 presents the studied cases of the double ellipse problem in this work, the mesh

characteristics and the order of accuracy of the [16] scheme. An exponential stretching was employed in the viscous simulations aiming to capture the main viscous flow characteristics, as for instance: circulation bubble formation, detachment and reattachment of the boundary layer, wake formation, etc. Table 4 presents the studied cases of the reentry capsule problem in this work, the mesh characteristics and the order of accuracy of [16].

**Table 3 Studied cases, mesh characteristics and accuracy order (Double ellipse problem).**

Case	Mesh	Accuracy Order
Inviscid – 2D	73x50	First <sup>a</sup>
Viscous – 2D	73x50 (7.5%) <sup>c</sup>	First <sup>a</sup>
Inviscid – 2D	73x50	Second <sup>a</sup>
Viscous – 2D	73x50 (7.5%)	Second <sup>a</sup>
Inviscid – 2D	73x50	First <sup>b</sup>
Viscous – 2D	73x50 (7.5%)	First <sup>b</sup>

<sup>a</sup> Structured spatial discretization; <sup>b</sup> Unstructured spatial discretization; <sup>c</sup> Exponential stretching.

**Table 4 Studied cases, mesh characteristics and accuracy order (Reentry capsule problem).**

Case	Mesh	Accuracy Order
Inviscid – 2D	65x50	First <sup>a</sup>
Viscous – 2D	65x50 (7.5%) <sup>b</sup>	First <sup>a</sup>
Inviscid – 2D	65x50	Second <sup>a</sup>
Viscous – 2D	65x50 (7.5%)	Second <sup>a</sup>

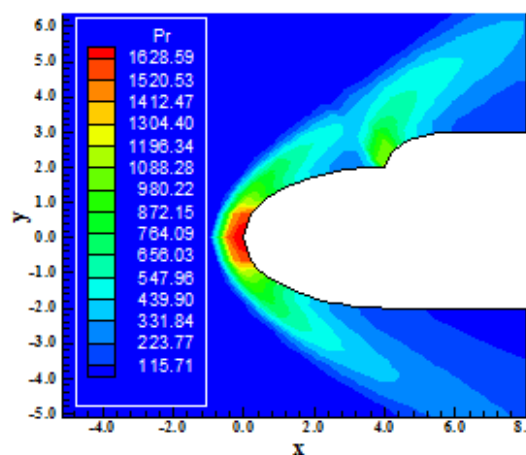
<sup>a</sup> Structured spatial discretization; <sup>b</sup> Exponential stretching.

#### 4.4 Results in Thermochemical Non-Equilibrium – Double Ellipse Case

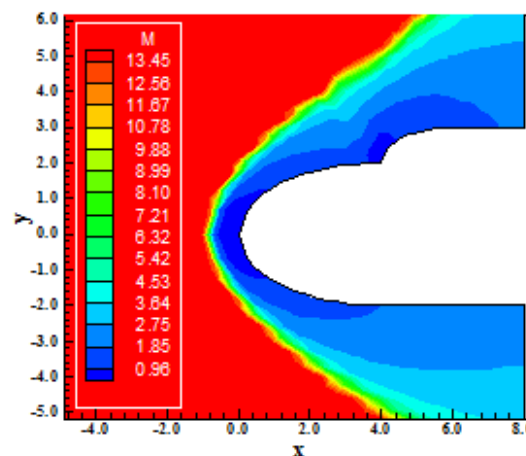
##### 4.4.1 Inviscid, structured and first order accurate case

Figure 7 exhibits the pressure contours around the double ellipse geometry calculated at the computational domain by the [16] scheme, in its first-order version, in thermochemical non-equilibrium. The non-dimensional pressure peak is equal to 1,628.59 unities and is located at the configuration nose. The shock wave at the configuration nose is normal. The second shock wave is weaker than the first one, as observed in the pressure contours. The solution presents good shock wave representations in both ellipses. Figure 8 shows the Mach number contours calculated at the computational domain. Regions of subsonic flows are formed behind the normal shock waves, at the

first and second ellipses. The shock wave develops normally: normal shock wave at the two ellipses, decaying to oblique shock waves and finally reaching, far from the double ellipse, the Mach wave. In reality, the second ellipse shock wave interacts with the first ellipse shock wave and retards this decaying to oblique shock waves. This occurs at the upper surface. At the lower surface, the shock wave is more curved, indicating the natural physical tendency to reach oblique shock wave behaviour.



**Figure 7. Pressure contours.**



**Figure 8. Mach number contours.**

Figure 9 presents the contours of the translational/rotational temperature distribution calculated at the computational domain. The translational/rotational temperature reaches a peak of 8,297 K at the configuration nose and determines an appropriated region to dissociation of N<sub>2</sub> and O<sub>2</sub>. Along the double ellipse, the translational/rotational temperature assumes an approximated value of 6,000 K, what also represents a good value to the

dissociation firstly of O<sub>2</sub> and, in second place, of the N<sub>2</sub>.

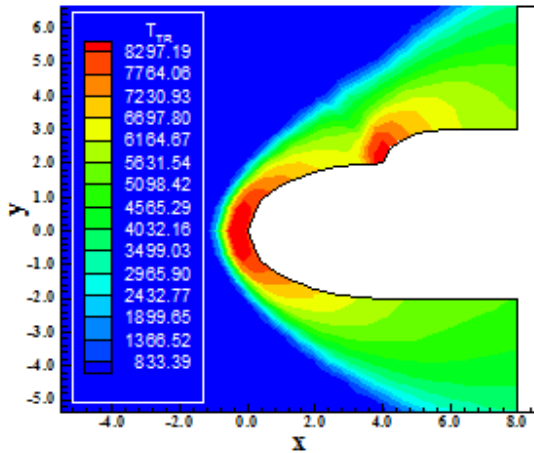


Figure 9. Translational/rotational temperature contours.

Figure 10 exhibits the contours of the vibrational temperature calculated at the two-dimensional computational domain. Its peak reaches a value of 7,305 K and also contributes to the dissociation of N<sub>2</sub> and O<sub>2</sub>, since the employed temperature to the calculation of the forward and backward reaction rates (reaction-rate-control temperature,  $T_{rrc}$ ) in the thermochemical non-equilibrium is equal to  $\sqrt{T \cdot T_v}$ , the square root of the product between the translational/rotational temperature and the vibrational temperature.

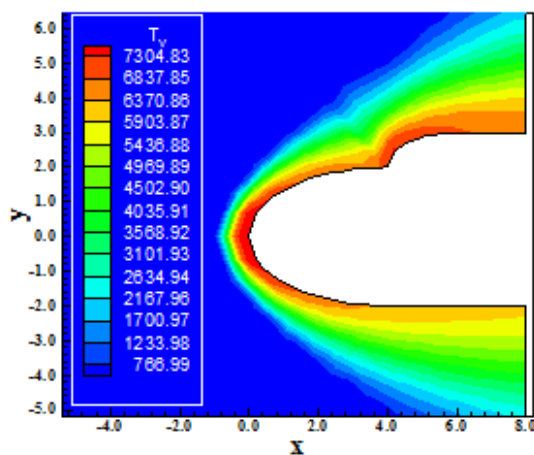


Figure 10. Vibrational temperature contours.

Hence, the effective temperature to the calculation of the chemical phenomena guarantees the couple between the vibrational mode and the dissociation reactions. In this configuration nose region, the temperature  $T_{rrc}$  reaches, in the steady state condition, the approximated value of 7,785 K,

guaranteeing that the dissociation phenomena described above occurs.

Figure 11 presents the velocity vector field around the double ellipse configuration. As can be seen, the tangency condition is well satisfied by the algorithm. The shock wave profile is also well captured.

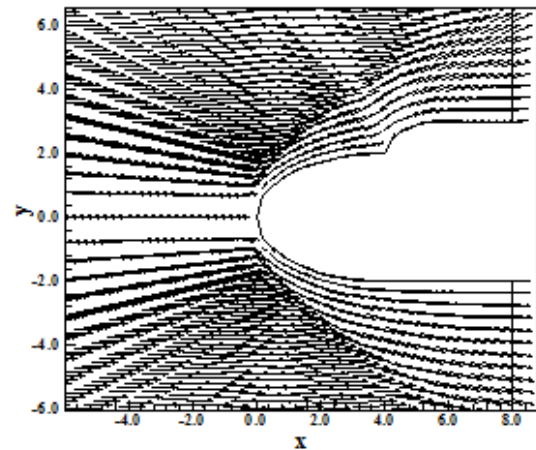


Figure 11. Velocity vector field.

Figure 12 shows the mass fraction distribution of the five chemical species under study, namely: N, O, N<sub>2</sub>, O<sub>2</sub> and NO, along the geometry stagnation line. As can be observed from this figure, enough dissociation of N<sub>2</sub> and O<sub>2</sub> occur, with the consequent meaningful increase of N, of NO and of O in the gaseous mixture. As mentioned early, this behaviour is expected due to the effective peak temperature reached at the calculation domain. The O presented the biggest absolute increase in its formation, whereas the N presented the biggest relative increase.

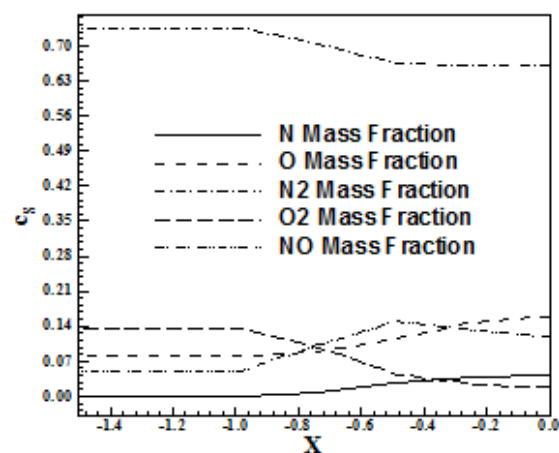


Figure 12. Mass fraction distribution at the double ellipse stagnation line.

**4.4.2 Viscous, structured and first order accurate case**

Figure 13 exhibits the pressure contours to the viscous reactive flow around a double ellipse, in two-dimensions, calculated at the computational domain. The non-dimensional pressure peak reaches 1,859 unities, more severe than that obtained with the inviscid case. The pressure field is also more severe in the viscous case than in the inviscid one. The shock is closer to the geometry due to the mesh exponential stretching and the viscous reactive effects of the simulation. The region of the pressure peak is also better defined.

Figure 14 shows the Mach number contours calculated at the computational domain. The subsonic flow regions, which are formed behind the normal shocks, are well captured and propagate by the lower and upper geometry walls, due to the transport phenomena considered in the viscous simulations. The shock waves present the expected behaviour: normal shock wave at the configuration nose, oblique shock waves and a Mach wave far from the double ellipse.

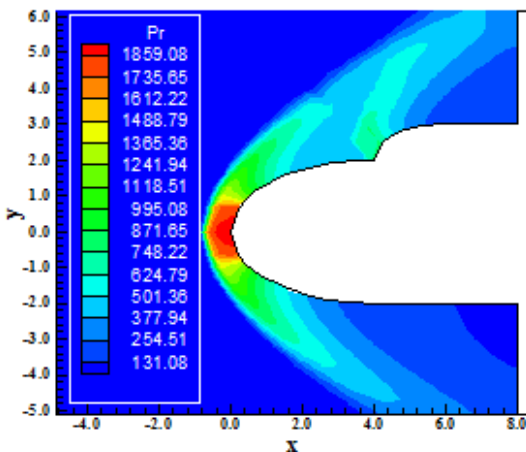


Figure 13. Pressure contours.

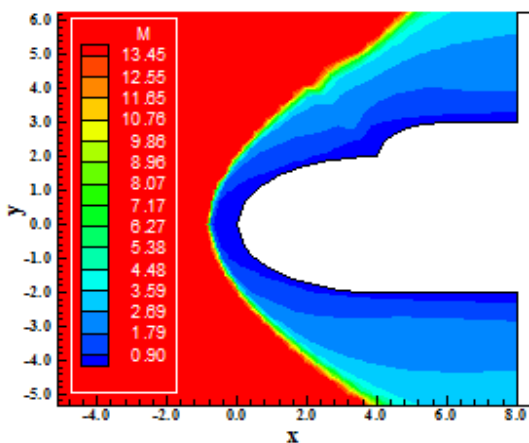


Figure 14. Mach number contours.

Figure 15 exhibits the distribution of the translational/rotational temperature calculated at the computational domain. The peak of translational/rotational temperature reaches the approximated value of 9,048 K at the configuration nose.

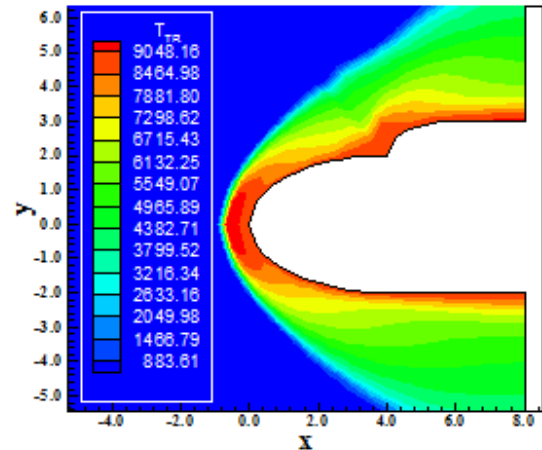


Figure 15. Translational/rotational temperature contours.

Figure 16 presents the vibrational temperature distribution calculated at the computational domain. Its peak, at the configuration nose, reaches an approximated value of 7,630 K. The effective temperature to the calculation of the dissociation and recombination reactions,  $T_{trc}$ , is equal approximately to 8,309 K, which guarantees that processes of dissociation of  $O_2$  and  $N_2$  can be captured by the employed formulation. This value of effective temperature to the viscous reactive simulations is superior to that obtained in the inviscid case.

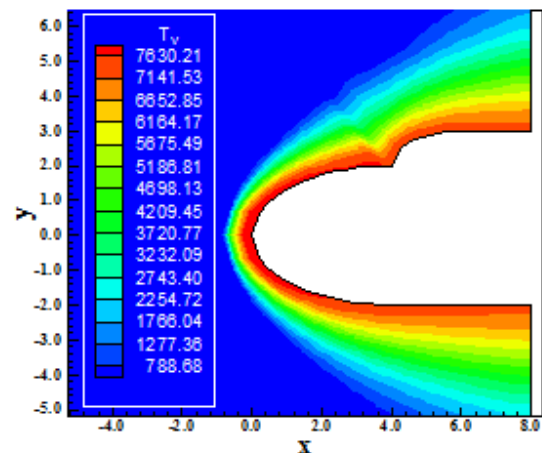


Figure 16. Vibrational temperature contours.

Figure 17 presents the velocity vector field around the double ellipse configuration. As can be

seen, the adherence and non-permeability conditions are well satisfied by the viscous formulation. The shock wave profile is also well captured.

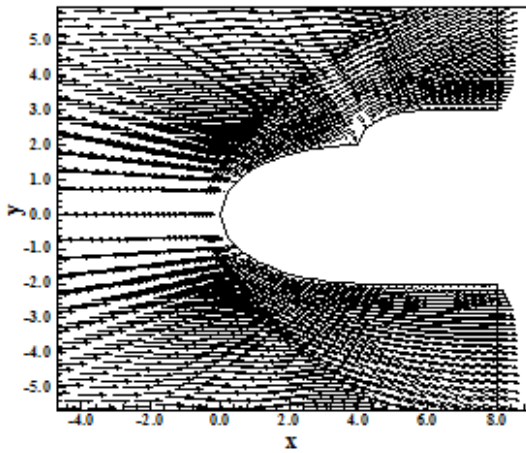


Figure 17: Velocity vector field.

Figure 18 exhibits the mass fraction distribution of the five chemical species under study along the geometry stagnation line. As can be observed, enough dissociation of the  $N_2$  and  $O_2$  occurs, with the consequent meaningful increase of the N, of the O, and of the NO in the gaseous mixture. This behaviour is expected due to the temperature peak reached in the calculation domain. The biggest absolute increase in the formation of a species was due to the O, while, in relative terms, was due to the N. As can also be noted, the mass fraction of the NO reaches a peak at approximately  $x = -0.4$  m and then reduces to a smaller value at the configuration nose. What is interesting is the smooth behaviour in which this peak is established, opposed to the inviscid peak behaviour.

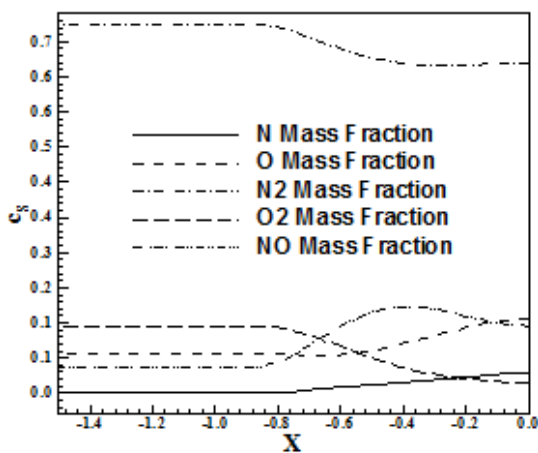


Figure 18. Mass fraction distribution at the double ellipse stagnation line.

#### 4.4.3 Inviscid, structured and second order accurate case

Figure 19 shows the pressure contours obtained by the inviscid simulation performed by the second-order [16] scheme employing a minmod non-linear flux limiter. The non-dimensional pressure peak is approximately equal to 1,724 unities, slightly superior to the respective peak obtained by the first-order solution. This pressure peak occurs at the configuration nose.

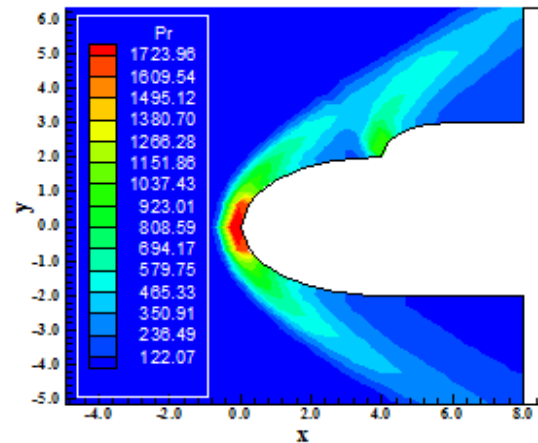


Figure 19. Pressure contours.

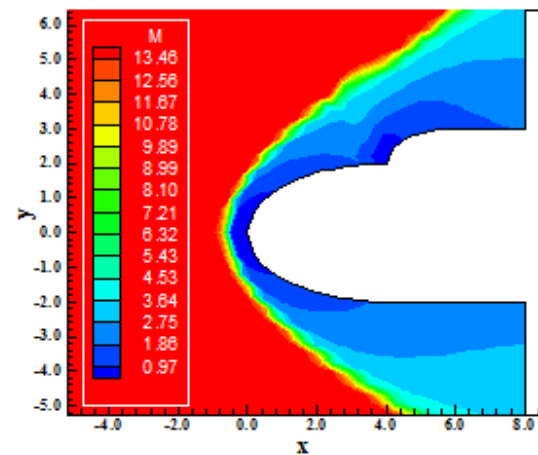


Figure 20. Mach number contours.

Figure 20 presents the Mach number contours obtained at the computational domain. The subsonic regions which are formed behind the normal shock waves are well characterized at the first and second ellipses. The shock wave originated at the configuration nose presents the expected behaviour, passing from a normal shock at the configuration stagnation line to a Mach wave far from the double ellipse.

Figure 21 exhibits the contours of the translational/rotational temperature distribution

calculated at the computational domain. The translational/rotational temperature peak occurs at the configuration nose and is approximately equal to 7,969 K.

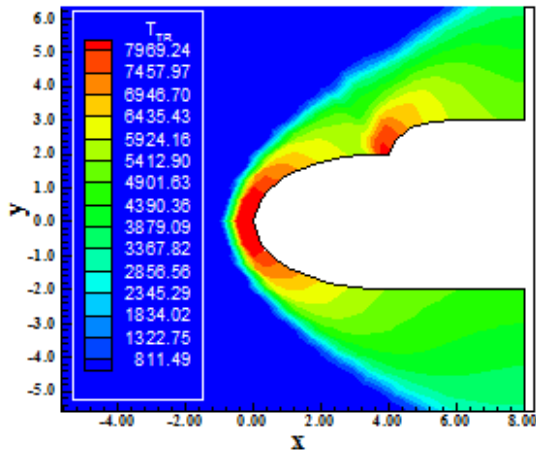


Figure 21. Translational/rotational temperature contours.

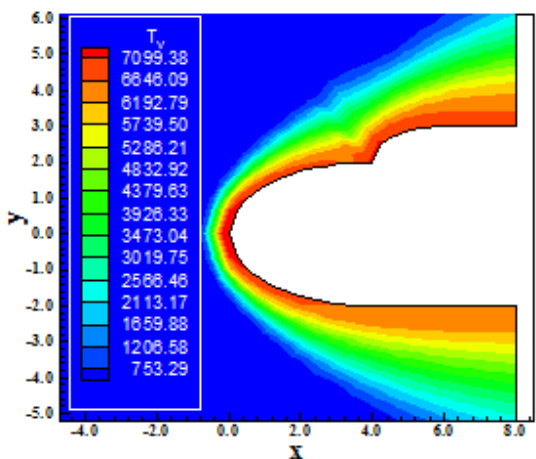


Figure 22. Vibrational temperature contours.

Figure 22 presents the contours of the vibrational temperature distribution calculated at the computational domain. The vibrational temperature peak is approximately equal to 7,099 K and is observed at the configuration nose. The effective temperature to calculation of the reaction rates (reaction rate control temperature,  $T_{rrc}$ ) is approximately equal to 7,521 K, which represents a temperature able to capture the dissociation phenomena of  $N_2$  and  $O_2$ .

Figure 23 presents the velocity vector field around the double ellipse configuration. As can be seen, the tangency condition is well satisfied by the inviscid formulation. The shock wave profile is also well captured.

Figure 24 exhibits the mass fraction distribution of the five chemical species under study, namely: N,

$O$ ,  $N_2$ ,  $O_2$  and  $NO$ , along the geometry stagnation line. As can be observed, considerable dissociation of  $N_2$  and  $O_2$  occurs, with consequent meaningful increase of the N, of the O and of the NO in the gaseous mixture. This behaviour is expected due to the effective temperature peak reached at the computational domain to the calculation of thermochemical non-equilibrium and to a second-order numerical formulation. Interesting enough is the NO solution which, opposed to the same analysis in [20], presents a decreased behaviour close to the geometry.

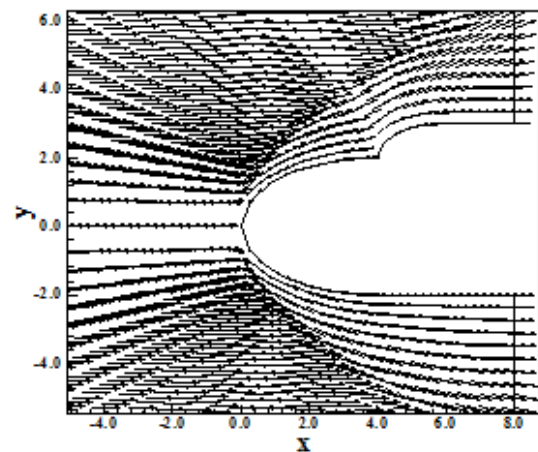


Figure 23. Velocity vector field.

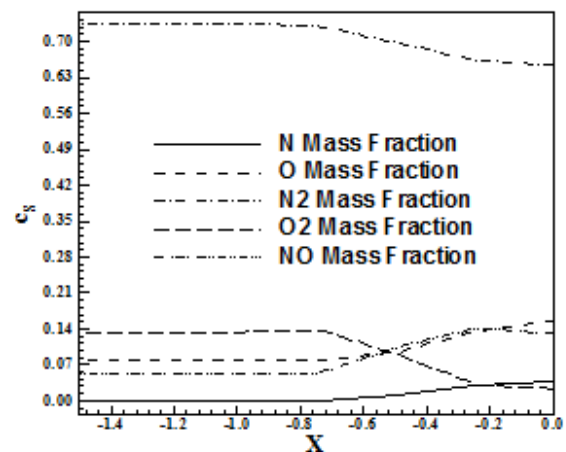


Figure 24. Mass fraction distribution at the double ellipse stagnation line.

#### 4.4.4 Viscous, structured and second order accurate case

Figure 25 exhibits the pressure contours calculated at the computational domain to the studied configuration of double ellipse. The non-dimensional pressure peak is approximately equal to 1,836 unities, less than the respective value obtained by the first order solution. The shock is positioned

closer to the blunt body due to the mesh stretching and the employed-viscous-reactive formulation.

and upper surfaces of the geometry is equal to 7,820 K. The effective temperature to the calculation of the reaction rates,  $T_{rrc}$ , was of 8,357 K, superior to that obtained with the first order solution, which is representative to the calculation of the  $N_2$  and  $O_2$  dissociations.

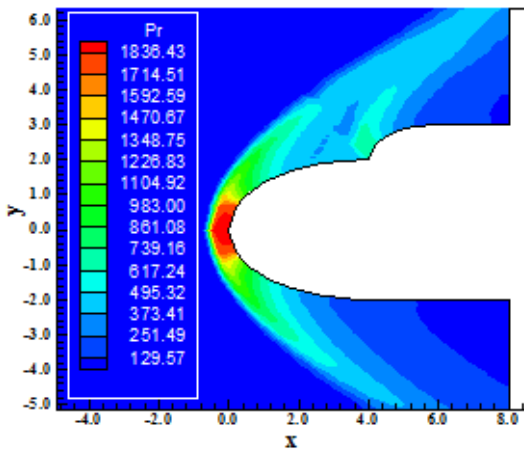


Figure 25. Pressure contours.

Figure 26 shows the Mach number contours obtained at the computational domain. The subsonic region behind the normal shock wave is well characterized and propagates along the lower and upper geometry surfaces, due to the consideration of the transport phenomena (viscosity, thermal conductivity and species diffusivities). The expected behavior to the shock wave is ratified: normal shock, oblique shocks and Mach wave. The shock wave behaviour is also the expected: normal shock at the geometry nose, oblique shock waves close to the configuration and Mach wave far from the geometry.

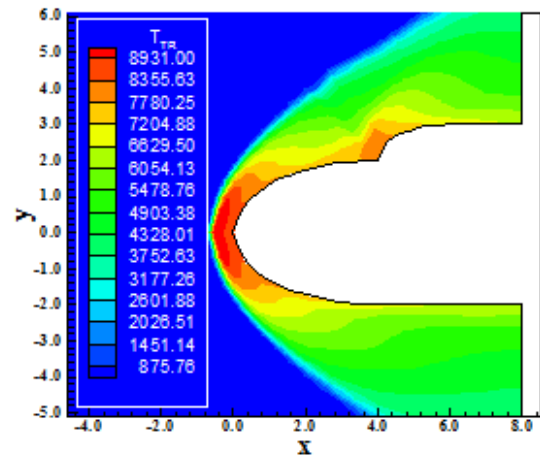


Figure 27. Translational/rotational temperature contours.

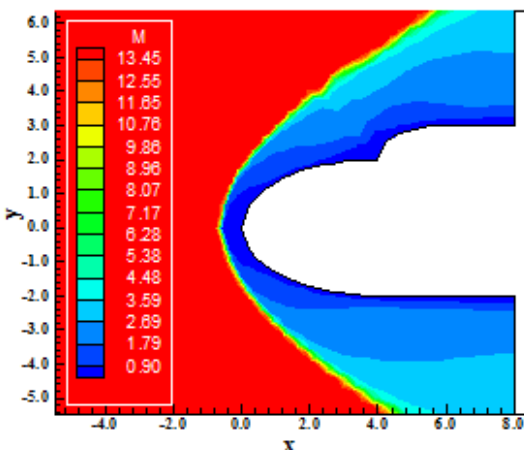


Figure 26. Mach number contours.

Figure 27 exhibits the translational/rotational temperature distribution calculated at the computational domain. The temperature peak at the configuration nose reaches 8,931 K. Figure 28 shows the vibrational temperature distribution calculated at the computational domain. The temperature peak at the nose and along the lower

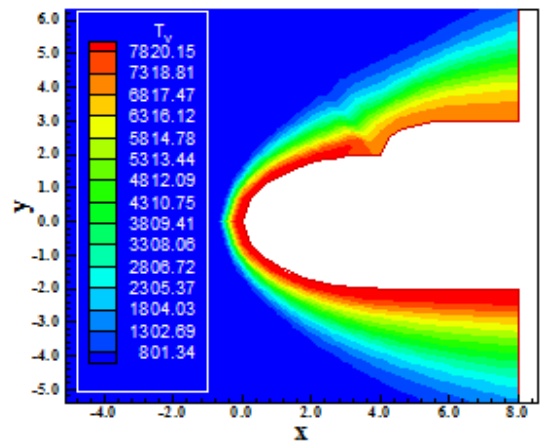


Figure 28. Vibrational temperature contours.

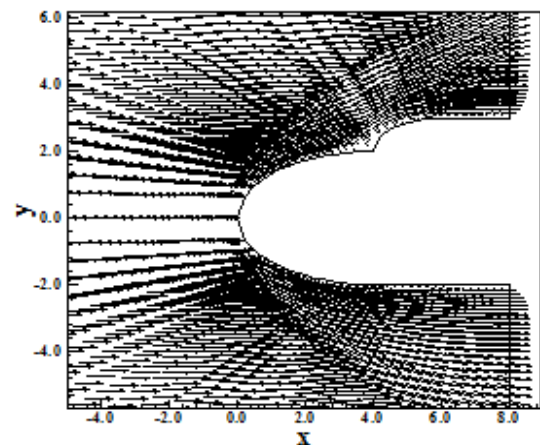


Figure 29. Velocity vector field.

Figure 29 presents the velocity vector field around the double ellipse configuration. As can be seen, the adherence and non-permeability conditions are well satisfied by the viscous formulation. The shock wave profile is also well captured.

Figure 30 presents the mass fraction distribution of the five chemical species under study, namely: N, O, N<sub>2</sub>, O<sub>2</sub> and NO, along the geometry stagnation line. As can be observed, good dissociation of N<sub>2</sub> and O<sub>2</sub> occurs, with consequent good increase of N, O and NO in the gaseous mixture. This behaviour is expected due to the effective temperature peak reached at the computational domain to the calculation of thermochemical non-equilibrium and to a second-order numerical formulation, which behaves in a more conservative way ([23]), providing major dissociation of N<sub>2</sub> and O<sub>2</sub>. In other words, this solution provided by the second-order [16] scheme, as seen in other cases, tends to originate bigger dissociation of N<sub>2</sub> and O<sub>2</sub>. As this solution is more precise (second-order), it should be considered as standard to comparison with other schemes. Again, it is possible to observe that the NO solution presents a smooth peak ahead of the nose configuration.

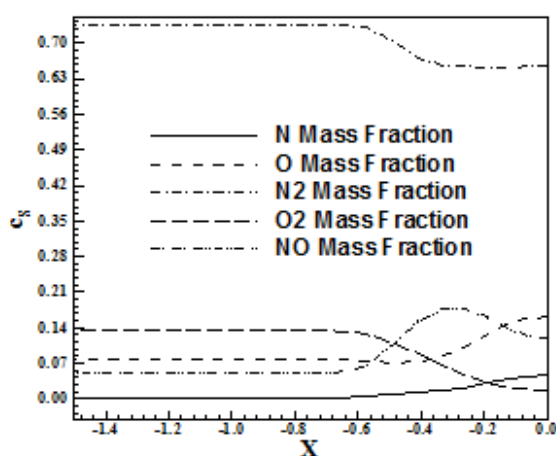


Figure 30. Mass fraction distribution at the double ellipse stagnation line.

#### 4.4.5 Inviscid, unstructured and first order accurate case

Figure 31 presents the pressure contours obtained by the inviscid simulation at the computational domain. The non-dimensional pressure peak, approximately 1,731 unities, is bigger than that obtained with the inviscid, first-order accurate in space, structured solution. This pressure peak occurs at the configuration nose. The second shock at the minor ellipse is well captured. Figure 32 exhibits the Mach number contours calculated at the computational

domain. The subsonic region behind the normal shock is well characterized, as also at the second shock, at the minor ellipse. The shock develops naturally.

Figure 33 shows the translational/rotational temperature distribution calculated at the computational domain. The temperature peak at the nose and at the configuration minor ellipse reaches approximately 8,913 K. Figure 34 presents the vibrational temperature distribution calculated at the computational domain. The temperature peak at the geometry nose is approximately equal to 6,678 K. The effective temperature to the calculation of the reaction rates (reaction rate control temperature,  $T_{\text{rrc}}$ ) was of 7,715 K, which is relevant to the calculation of N<sub>2</sub> and O<sub>2</sub> dissociations. This effective temperature,  $T_{\text{rrc}}$ , is smaller than that obtained to the inviscid, structured, first-order accurate case and, therefore, a minor number of N<sub>2</sub> and O<sub>2</sub> dissociations are expected. The shock wave in both figures present the expected behavior: passing from a normal shock to oblique shocks and finishing with a Mach wave.

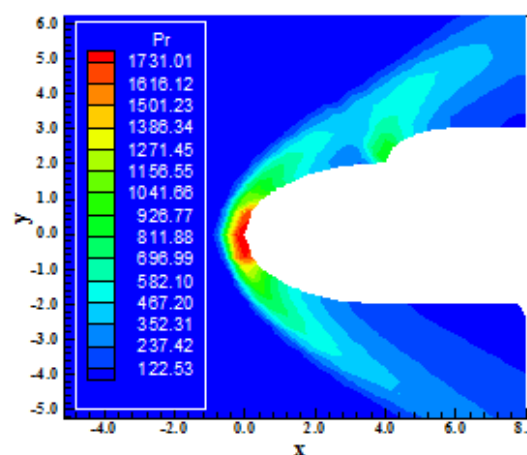


Figure 31. Pressure contours.

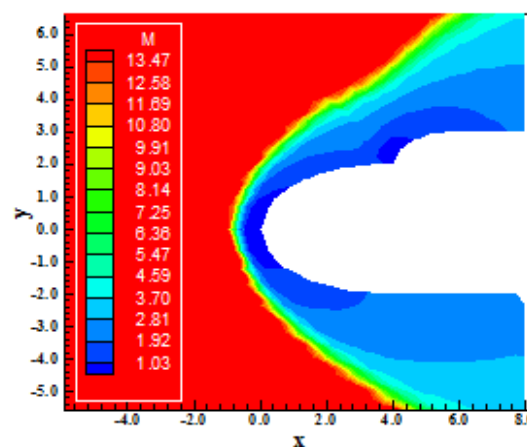


Figure 32. Mach number contours.

**4.4.6 Viscous, unstructured and first order accurate case**

Figure 36 exhibits the pressure contours calculated at the computational domain. The non-dimensional pressure peak, approximately 1,881 unities, is slightly superior to the respective one obtained from the structured, first-order accurate solution. The pressure peak occurs at the configuration nose, where the normal shock occurs. The second shock at the minor ellipse is well captured.

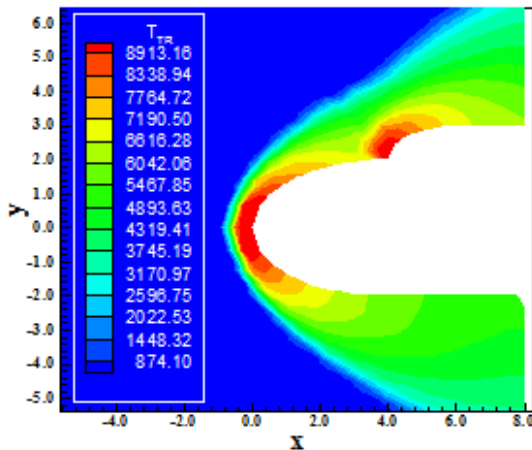


Figure 33. Translational/rotational temperature contours.

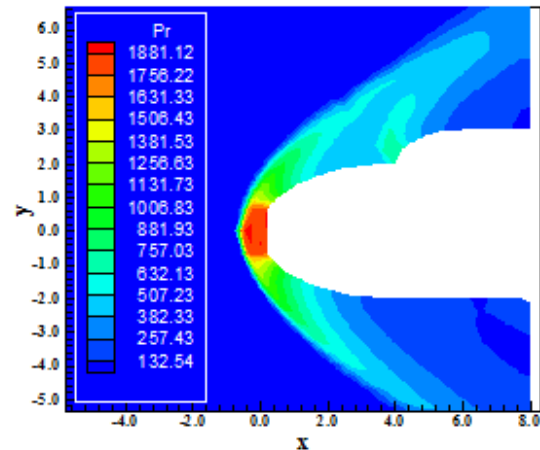


Figure 36. Pressure contours.

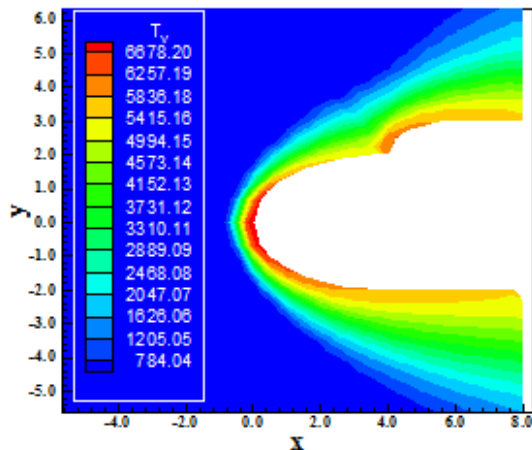


Figure 34. Vibrational temperature contours.

Figure 35 shows the velocity vector field to an inviscid flow. The flow tangency condition is well guaranteed by the employed inviscid formulation.

Figure 37 presents the Mach number contours calculated at the computational domain. The subsonic flow region, behind the frontal shock, is well characterized along the geometry, due to effects of transport phenomena (viscosity, thermal conductivity and gaseous diffusion). The shock behavior is also the expected: normal shock developing to oblique shock waves and finishing in a Mach wave.

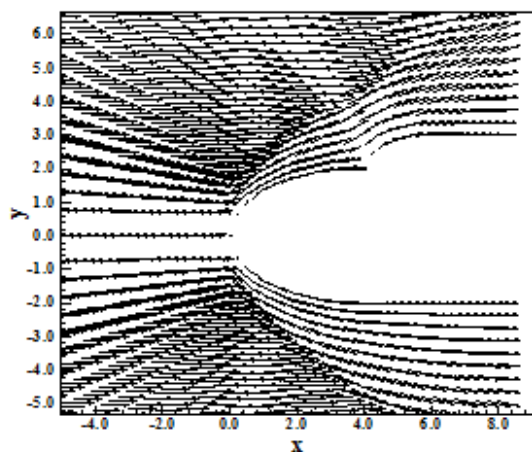


Figure 35. Velocity vector field.

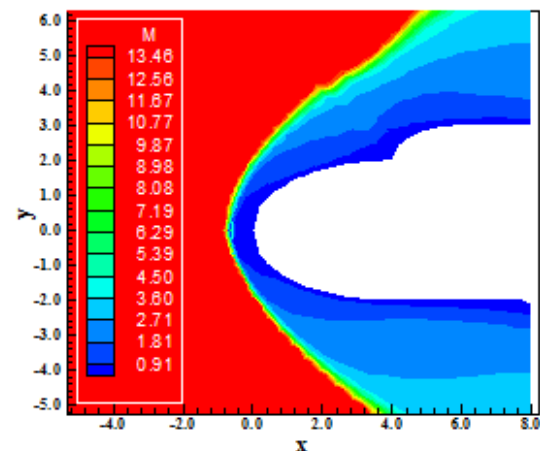


Figure 37. Mach number contours.

Figure 38 shows the translational/rotational temperature distribution calculated at the computational domain. The temperature peak at the configuration nose reaches approximately 9,323 K. Figure 39 exhibits the vibrational temperature distribution calculated at the computational domain. The temperature peak at the geometry nose is approximately equal to 7,239 K. The effective temperature to the calculation of the reaction rates,  $T_{rec}$ , was of 8,215 K, which is considerable to the calculation of the  $N_2$  and  $O_2$  dissociations. This effective temperature is less than that obtained to the viscous, structured, first-order accurate case and, therefore, a minor number of  $N_2$  and  $O_2$  dissociations are expected. The shock wave in both figures presents the expected behavior: normal shock, oblique shock waves and a Mach wave.

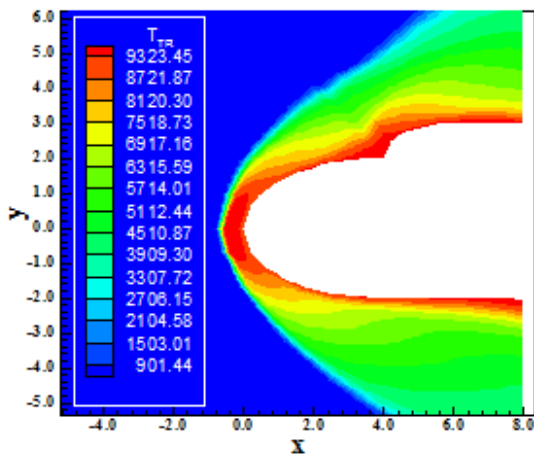


Figure 38. Translational/rotational temperature contours.

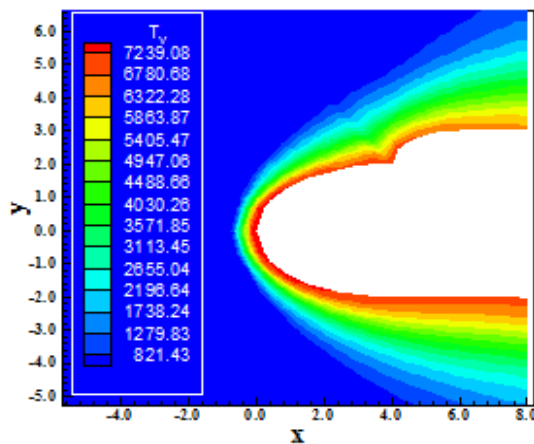


Figure 39. Vibrational temperature contours.

Figure 40 exhibits the velocity vector field to a viscous flow formulation. A small detachment and reattachment of the boundary layer at the minor ellipse occurs. The adherence and impermeability

conditions are guaranteed by the viscous formulation.

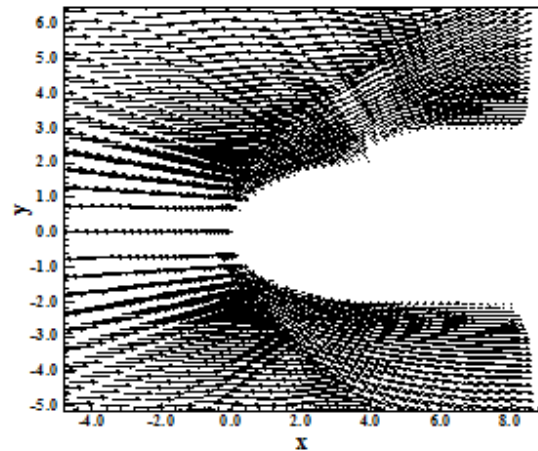


Figure 40. Velocity vector field.

#### 4.5 Results in Thermochemical Non-Equilibrium – Reentry Capsule Case

##### 4.5.1 Inviscid, structured and first order accurate case

Figure 41 exhibits the pressure contours to the reentry capsule configuration calculated at the computational domain. The non-dimensional pressure peak is approximately equal to 1,269 unities. The solution presents good symmetry characteristics. Figure 42 presents the Mach number contours calculated at the computational domain. A subsonic flow region is formed behind the normal shock wave at the geometry stagnation line. The shock wave develops normally: pass from a normal shock wave, at the geometry stagnation line, to oblique shock waves, finishing with a Mach wave. Good symmetry characteristics are observed.

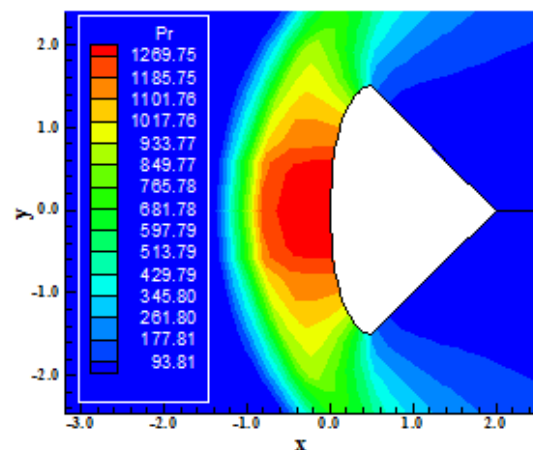


Figure 41. Pressure contours.

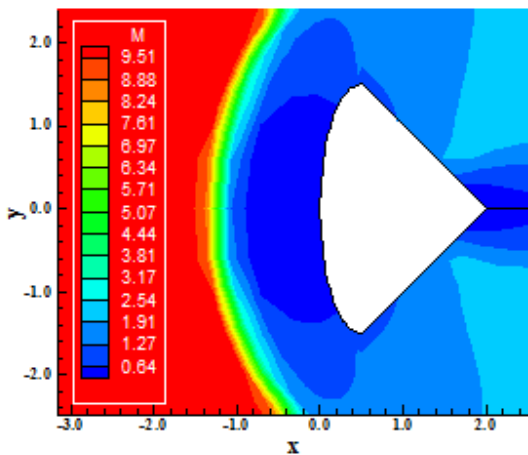


Figure 42. Mach number contours.

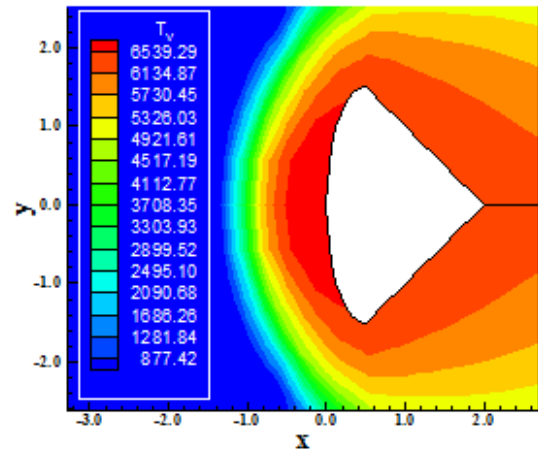


Figure 44. Vibrational temperature contours.

Figure 43 shows the translational/rotational temperature distribution calculated at the computational domain. The temperature peaks occur at the configuration nose and at the configuration trailing edge. This peak of translational/rotational temperature is approximately equal to 7,290 K. Figure 44 exhibits the vibrational temperature distribution calculated at the computational domain. The peak of vibrational temperature occurs at the configuration nose and is approximately equal to 6,539 K. The reaction rate control temperature,  $T_{rrc}$ , is approximately equal to 6,904 K, which is considerable to the  $O_2$  dissociation, mainly, and to the  $N_2$ . Both solutions, Figures 43 and 44, present good symmetry properties.

Figure 45 presents the velocity vector field to the inviscid case. As can be observed, the tangency condition is well satisfied. The velocity vector is tangent along all the configuration walls.

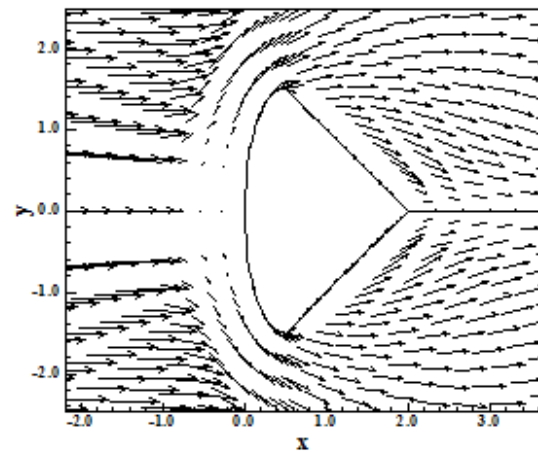


Figure 45. Velocity vector field.

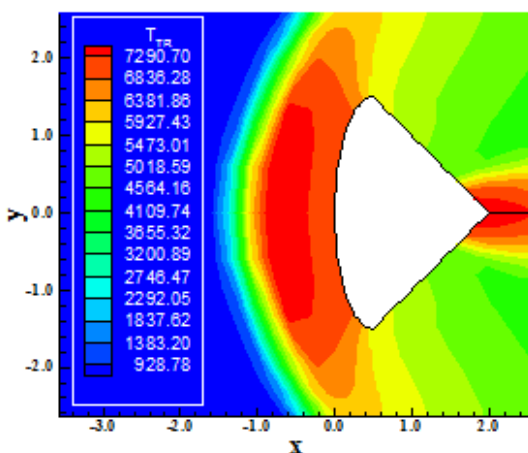


Figure 43. Translational/rotational temperature contours.

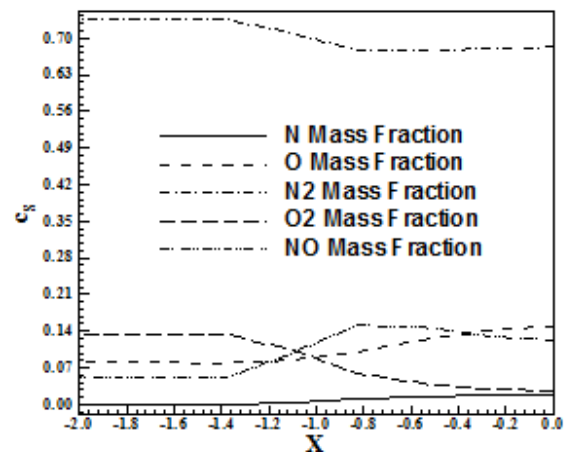


Figure 46. Mass fraction distribution at the reentry capsule stagnation line.

Figure 46 exhibits the mass fraction distribution of the five chemical species studied in this work, namely: N, O,  $N_2$ ,  $O_2$  and NO, along the geometry stagnation line. Good dissociations of  $N_2$  and  $O_2$

occurs close to the configuration nose. Good formations of N, in relation to its initial value, and of O occur. There is also a good formation of NO at the stagnation line, at the post-shock region, presenting the biggest absolute variation among the formed species. Meaningful formations were reached with an effective temperature little above 6,904 K. This is the behavior presented to the structured, inviscid, first-order accurate in space, solution.

**4.5.2 Viscous, structured and first order accurate case**

Figure 47 exhibits the pressure contours calculated at the computational domain to the reentry capsule problem submitted to viscous flow. A structured, first-order formulation is employed in this simulation. The non-dimensional pressure peak is equal to 1,387 unities, bigger than that obtained in the inviscid, structured, first-order solution. The pressure field in this case is more severe than that of the inviscid one. Good symmetry properties are observed.

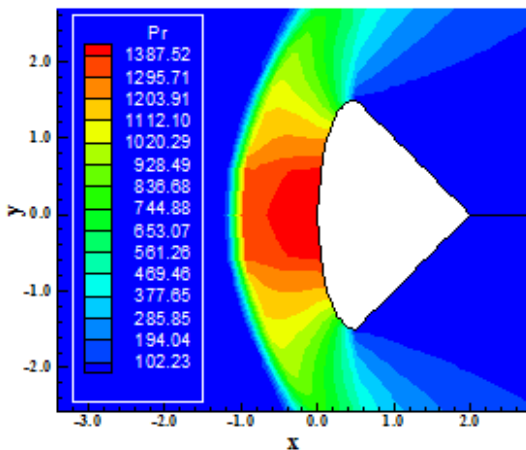


Figure 47. Pressure contours.

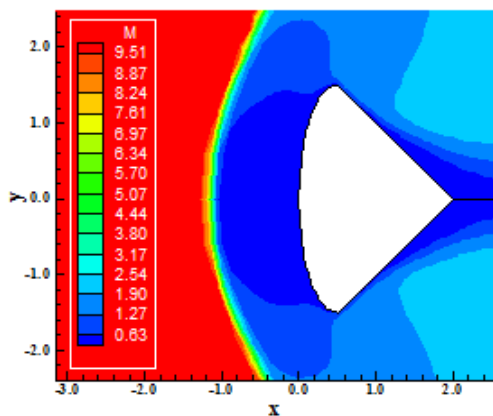


Figure 48. Mach number contours.

Figure 48 shows the Mach number contours calculated at the computational domain. The solution presents a subsonic flow region at the configuration nose, behind the normal shock. The extension of this region depends of the flow properties (Mach number, pressure, etc.) and of the geometry characteristics. This subsonic flow region propagates around all geometry due to the transport phenomena originated by the viscous formulation. At the geometry trailing edge appears a viscous wake, where a great loss of flow energy and the formation of circulation bubbles are predominant. The shock develops normally: normal shock at the geometry stagnation line, oblique shock waves along the configuration and Mach wave far from the geometry. Good characteristics of symmetry are observed in the solution.

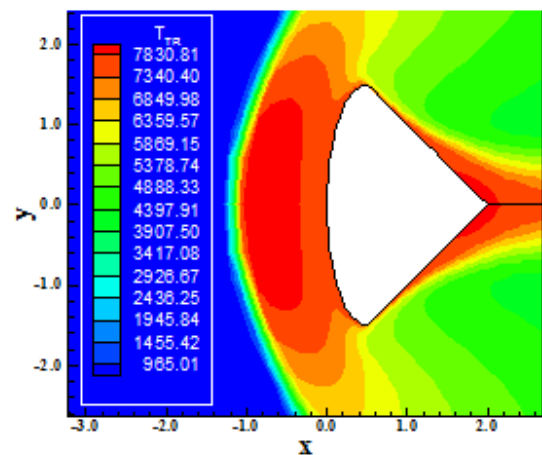


Figure 49. Translational/rotational temperature contours.

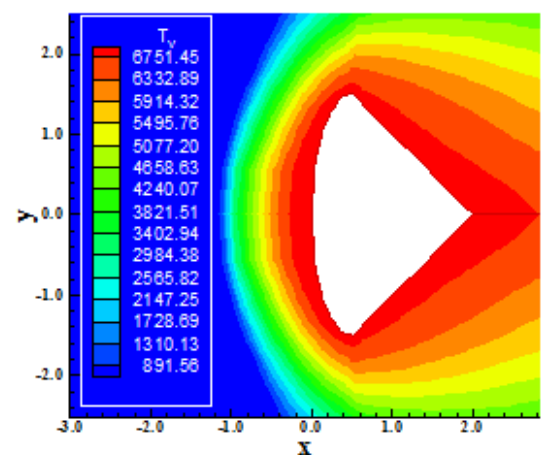


Figure 50. Vibrational temperature contours.

Figure 49 presents the contours of the translational/rotational temperature distribution calculated at the computational domain. The peak of the translational/rotational temperature occurs close

to the configuration nose and at the viscous wake at the geometry trailing edge. The peak value of this temperature is approximately equal to 7,830 K.

Figure 50 exhibits the contours of the vibrational temperature distribution calculated at the computational domain. The vibrational temperature peak occurs close to the configuration nose. This peak is approximately equal to 6,751 K. The effective temperature to be employed in the chemical model,  $T_{trc}$ , is approximately equal to 7,271 K, which indicates meaningful  $N_2$  and  $O_2$  dissociation phenomena. Figures 49 and 50 present good symmetry characteristics.

Figure 51 shows the velocity vector field to this viscous flow. As mentioned earlier, there is the formation of a boundary layer separation region, with the formation of a pair of circulation bubbles. These bubbles are well captured by the solution. In this region there is a great loss of energy. This energy is dissipated through the circulation bubble structures. The adherence and impermeability conditions are guaranteed by the viscous formulation. Good symmetry characteristics are observed.

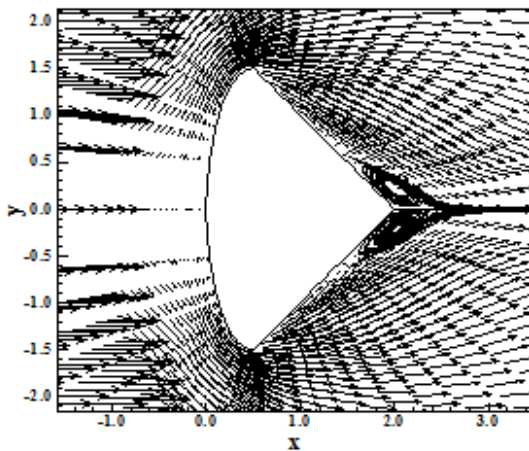


Figure 51. Velocity vector field and streamlines.

Figure 52 presents the mass fraction distribution of the five chemical species studied in this work, namely: N, O,  $N_2$ ,  $O_2$  and NO along the geometry stagnation line. Good dissociations of  $N_2$  and  $O_2$  occur with both reaching a constant value close to the geometry nose. Good formations of N, in relation to its initial value, and of O. It is also seen a good formation of the NO at the stagnation line, at the post-shock region, presenting the biggest absolute variation among the species that were formed. Meaningful formations were reached with an effective temperature little bigger than 7,270 K. This is the behavior presented to the structured, viscous, first-order accurate in space, solution.

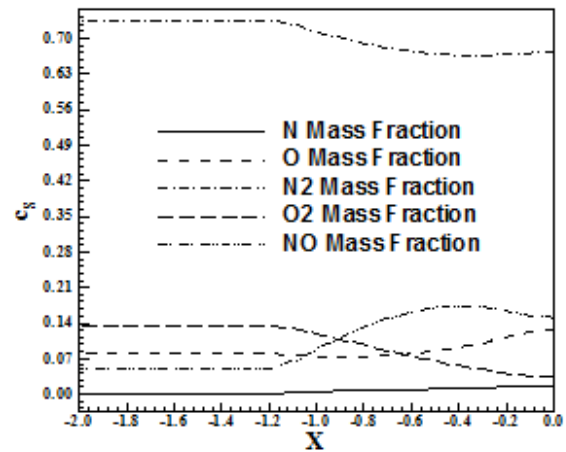


Figure 52. Mass fraction distribution at the reentry capsule stagnation line.

#### 4.5.3 Inviscid, structured and second order accurate case

Figure 53 exhibits the pressure contours calculated at the computational domain to the inviscid, structured, second-order accurate in space, case. This second-order accuracy is obtained by the [16] scheme employing a TVD “MUSCL” procedure, with minmod non-linear limiter. The non-dimensional pressure peak is approximately equal to 1,312 unities, superior to the respective peak obtained by the inviscid, first-order accurate, solution. The pressure field also is more severe than the respective field of the inviscid, first-order accurate, solution. The pressure peak occurs at the configuration nose. Good symmetry characteristics are observed in the figure.

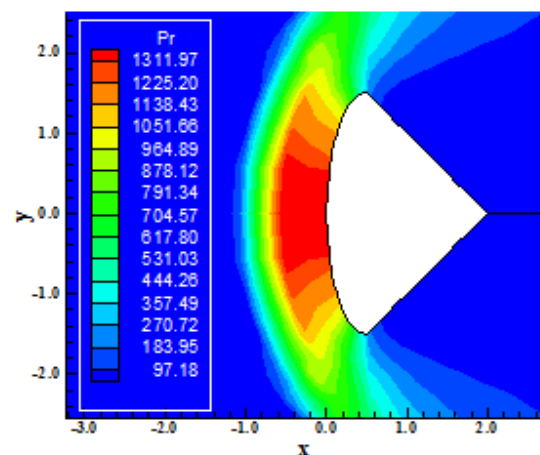


Figure 53. Pressure contours.

Figure 54 shows the Mach number contours calculated at the computational domain. A vast

region of subsonic flow is formed at the configuration nose, behind the normal shock. This region is formed by the shock intensity and its extension depends on the flow properties (Mach number, pressure, etc.) and on the geometry characteristics. The shock wave develops normally: normal shock wave at the symmetry line, oblique shock waves along the configuration and Mach wave far from the geometry. Good symmetry characteristics are observed in the solution.

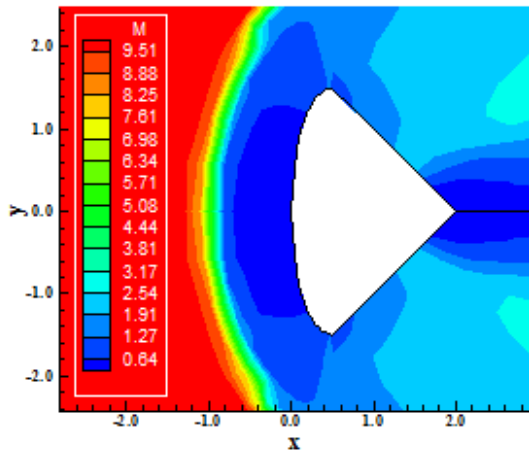


Figure 54. Mach number contours.

Figure 55 presents the translational/rotational temperature distribution calculated at the computational domain. The translational/rotational pressure peak occurs at the configuration nose and is approximately equal to 7,094 K.

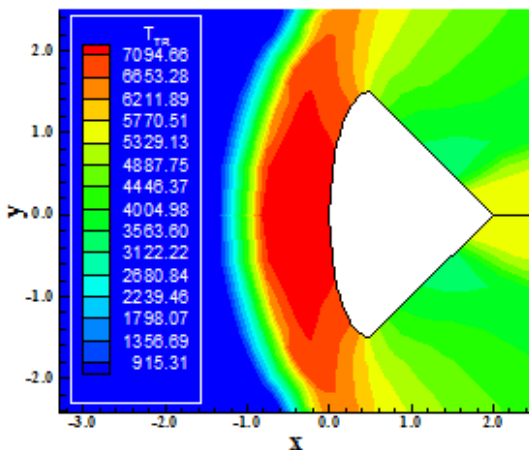


Figure 55. Translational/rotational temperature contours.

Figure 56 exhibits the vibrational temperature distribution calculated at the computational domain. The vibrational temperature peak occurs at the configuration nose and is approximately equal to 6,539 K. The effective temperature to be considered

to the chemical formulation,  $T_{trc}$ , is approximately equal to 6,811 K, which is meaningful to capture the  $N_2$  and  $O_2$  dissociations. This temperature is smaller than the respective one obtained by the inviscid, first-order accurate, solution and indicates that minor  $N_2$  and  $O_2$  dissociations should occur.

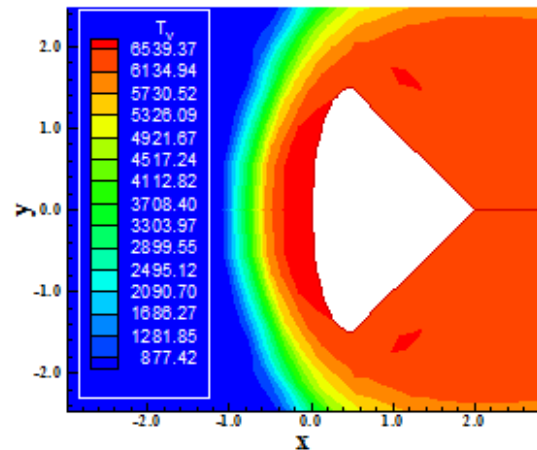


Figure 56. Vibrational temperature contours.

Figure 57 presents the velocity vector field to this inviscid flow case calculated with the second-order accurate [16] scheme. The tangency condition is guaranteed by the inviscid formulation. Good symmetry characteristics are also observed.

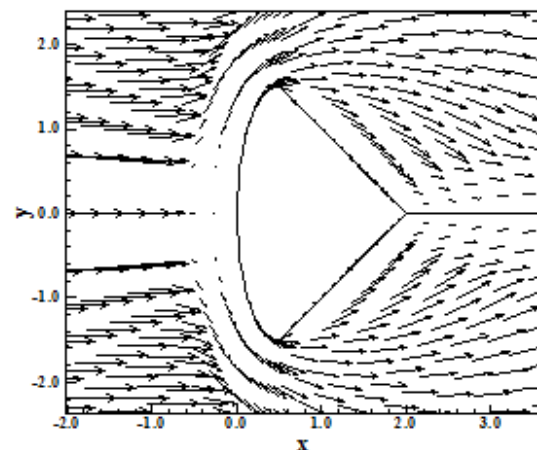


Figure 57. Velocity vector field.

Figure 58 exhibits the mass fraction distribution of the five chemical species studied in this work along the geometry stagnation line. Good  $N_2$  and  $O_2$  dissociations occur, with the  $N_2$  reaching a constant value close to the configuration nose. Good formations of N, in relation to its initial value, and of O and of NO, with the O presenting the biggest variation among the formed species, occur. With it, it is possible to affirm that meaningful formations

were reached with an effective temperature of 6,811 K (smaller than in the inviscid, first-order accurate, case). This is the behavior presented to the structured, inviscid, second-order accurate in space, solution.

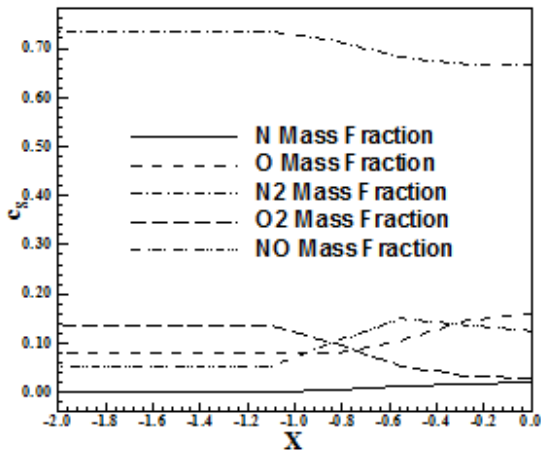


Figure 58. Mass fraction distribution at the reentry capsule stagnation line.

4.5.4 Viscous, structured and second order accurate case

Figure 59 presents the pressure contours calculated at the computational domain to the structured, viscous, second-order accurate, case. The non-dimensional pressure peak reaches an approximated value of 1,351 unities, inferior to the respective one obtained in the viscous, first-order accurate, solution. The pressure peak is located at the configuration nose. The pressure field is also globally less severe. Good symmetry characteristics are observed in the solution.

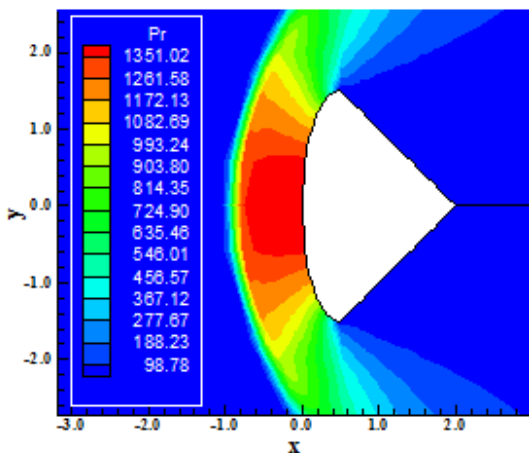


Figure 59. Pressure contours.

Figure 60 exhibits the Mach number contours calculated at the computational domain. A subsonic

flow region, observed in the other solutions too, is formed at the configuration nose, behind the frontal shock. This subsonic flow region propagates around the reentry capsule geometry until the trailing edge. The extension of the subsonic region at the configuration nose depends on the flow properties and on the geometry characteristics. At the configuration trailing edge, a viscous wake is formed, where the formation of circulation bubbles occurs, as seen earlier. This region is typically of great loss of energy and pressure. Good symmetry characteristics are observed.

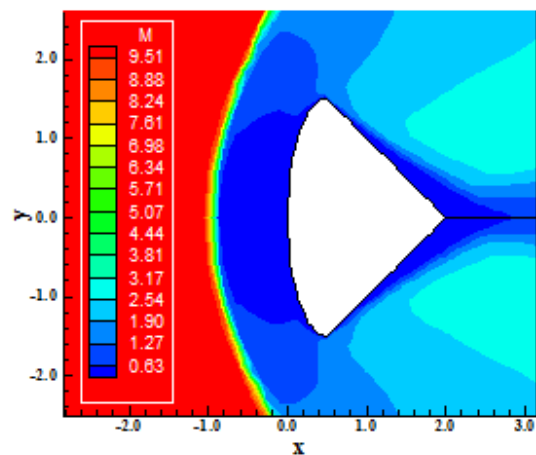


Figure 60. Mach number contours.

Figure 61 shows the contours of the translational/rotational temperature distribution calculated at the computational domain. The translational/rotational temperature peak assumes the approximated value of 7,788 K, close to the geometry nose. Figure 62 presents the vibrational temperature distribution calculated at the computational domain. The vibrational temperature peak occurs also close to the configuration nose and reaches the approximate value of 7,487 K. The effective temperature to be considered in the chemical calculations,  $T_{trc}$ , reaches the approximated value of 7,636 K, which is an appropriated temperature to promote the  $N_2$  and  $O_2$  dissociations close to the reentry capsule geometry. This temperature is superior to that obtained to the viscous, first-order accurate, case and, with it, more  $N_2$  and  $O_2$  dissociations are expected.

Figure 63 exhibits the velocity vector field calculated at the computational domain. As can be observed, the boundary layer detachment at the trailing edge region of the reentry capsule and the formation of a pair of circulation bubbles due to the viscous phenomena and due to the adverse pressure gradient in this region occur. Good symmetry characteristics are observed in the solution.

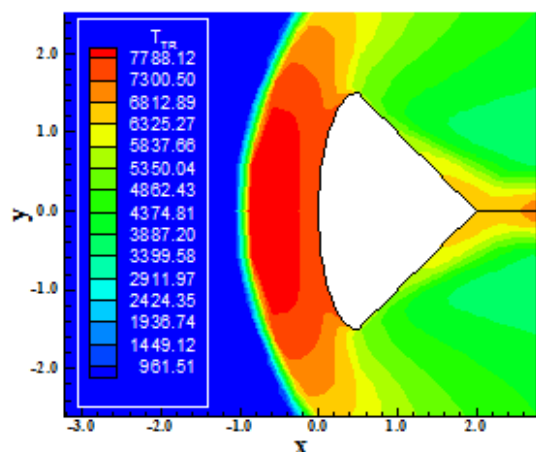


Figure 61. Translational/rotational temperature contours.

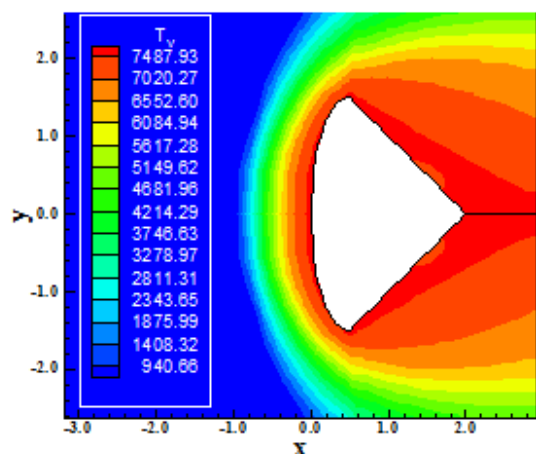


Figure 62. Vibrational temperature contours.

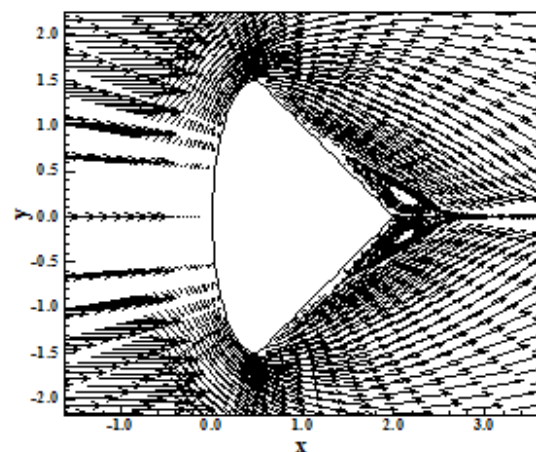


Figure 63. Velocity vector field and streamlines.

Figure 64 shows the mass fraction distribution of the five chemical species studied in this work, namely: N, O, N<sub>2</sub>, O<sub>2</sub> and NO along the geometry stagnation line. A slight N<sub>2</sub> dissociation occurs, whereas good dissociation of O<sub>2</sub> close to the

configuration nose happens. Good formation of N, in relation to its initial value, and good formation of O occurs. It is also seen a good formation of NO along the stagnation line, at the post-shock region. The increase at the formation of NO would be bigger than that of the O, whether a reduction in relation to its initial behavior has not occurred. This reduction in the NO mass fraction close to the geometry nose is due to the constancy reached in this region by the N<sub>2</sub> and O<sub>2</sub> dissociations and due to the increase in the formation of the N and of O. Even so, meaningful formations were reached with an effective temperature little bigger than 7,600 K, although with minor N and NO formations than those obtained with the viscous, first-order accurate, case. In this last case, a bigger effective temperature,  $T_{trc}$ , was reached. This is the behavior presented by the viscous, structured, second-order accurate in space, solution.

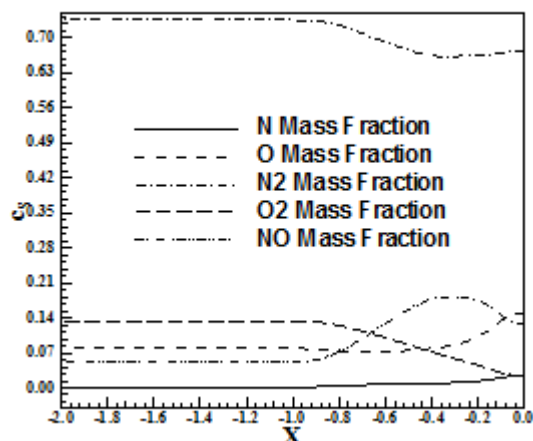


Figure 64. Mass fraction distribution at the reentry capsule stagnation line.

#### 4.6 Shock Position of the Double Ellipse Case (Shock at the Nose)

In this section is presented the behavior of the shock position in ideal, in thermal equilibrium and chemical non-equilibrium ([23]), and in thermochemical non-equilibrium conditions. Only first-order solutions are compared because the second-order ideal gas solutions did not present converged ones.

The detached shock position in terms of pressure distribution, in the inviscid case and first-order accurate solution, is exhibited in Fig. 65. It is shown the ideal-gas-shock position, the thermal equilibrium and chemical non-equilibrium shock position ([23]), and the thermochemical non-equilibrium shock position. As can be observed, the ideal-gas-shock position is located at 1.20 m,

whereas the thermal equilibrium and chemical non-equilibrium and the thermochemical non-equilibrium positions are located at 1.00 m. As referred in the CFD literature, in reactive flow the shock is closer to the configuration. As can be observed in this inviscid solution, the reactive shocks are actually closer to the double ellipse than the ideal shock.

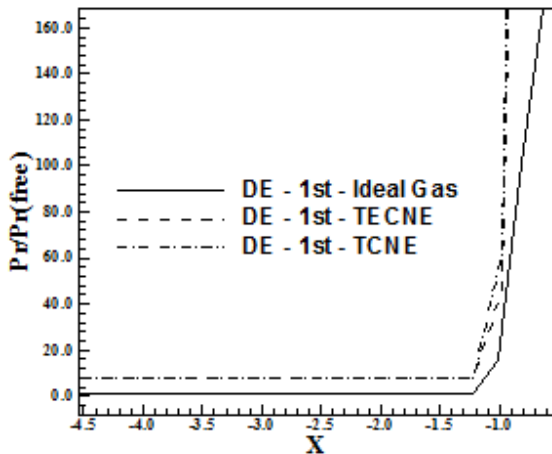


Figure 65. Shock position (Inviscid case).

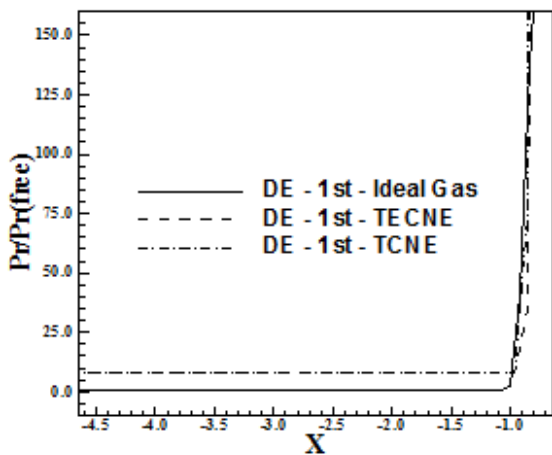


Figure 66. Shock position (Viscous case).

The detached shock position in terms of pressure distribution, in the viscous case and first-order accurate solution, is exhibited in Fig. 66. It is shown the ideal-gas-shock position, the thermal equilibrium and chemical non-equilibrium shock position ([23]), and the thermochemical non-equilibrium shock position. As can be observed, the ideal-gas-shock position is located at 1.0 m, whereas the thermal equilibrium and chemical non-equilibrium and the thermochemical non-equilibrium positions are located at 0.80 m. As mentioned above, in reactive flow the shock is closer to the configuration. As can be observed in

this viscous solution, the reactive shock is actually closer to the double ellipse than the ideal shock.

#### 4.7 Shock Position of the Reentry Capsule Case (Shock at the Nose)

In this section is presented the behavior of the shock position in ideal, in thermal equilibrium and chemical non-equilibrium ([23]), and in thermochemical non-equilibrium conditions. Only first-order solutions are compared because the second-order ideal gas solutions did not present converged ones.

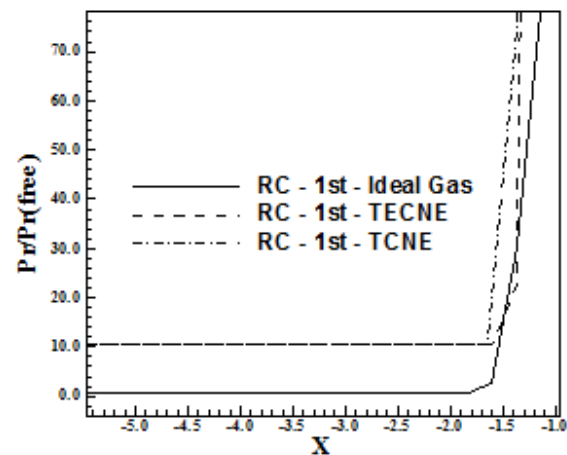


Figure 67. Shock position (Inviscid case).

The detached shock position in terms of pressure distribution, in the inviscid case and first-order accurate solution, is exhibited in Fig. 67. It is shown the ideal-gas-shock position, the thermal equilibrium and chemical non-equilibrium shock position ([23]), and the thermochemical non-equilibrium shock position. As can be observed, the ideal-gas-shock position is located at 1.60 m, whereas the thermal equilibrium and chemical non-equilibrium and the thermochemical non-equilibrium positions are located at 1.40 m. As referred in the CFD literature, in reactive flow the shock is closer to the configuration. As can be observed in this inviscid solution, the reactive shocks are actually closer to the reentry capsule than the ideal shock.

The detached shock position in terms of pressure distribution, in the viscous case and first-order accurate solution, is exhibited in Fig. 68. It is shown the ideal-gas-shock position, the thermal equilibrium and chemical non-equilibrium shock position ([23]), and the thermochemical non-equilibrium shock position. As can be observed, the ideal-gas-shock position is located at 1.35 m, whereas the thermal equilibrium and chemical non-

equilibrium and the thermochemical non-equilibrium positions are located at 1.25 m. As mentioned above, in reactive flow the shock is closer to the configuration. As can be observed in this viscous solution, the reactive shock is actually closer to the reentry capsule than the ideal shock.

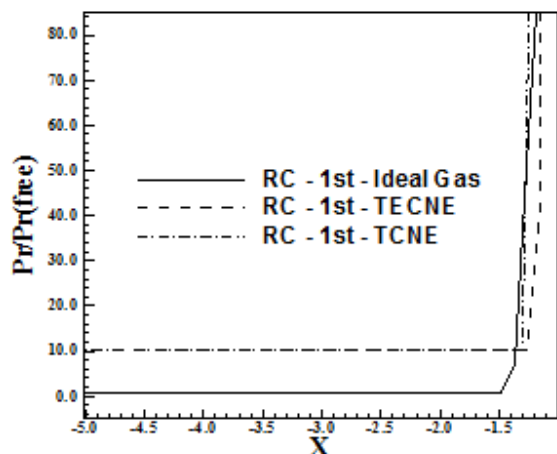


Figure 68. Shock position (Viscous case).

#### 4.8 Aerodynamic Coefficients of Lift and Drag

Table 5 exhibits the aerodynamic coefficients of lift and drag obtained by the problem of the double ellipse, with structured discretization, to the reactive formulations. Both reactive formulations of thermal equilibrium and chemical non-equilibrium ([22-23; 34]) and thermochemical non-equilibrium are considered in this comparison. These coefficients are due to the pressure term alone. The contribution of the friction term was not considered.

Table 5 Aerodynamic coefficients of lift and drag to the structured double ellipse case.

Studied Case	$c_L$	$c_D$
1 <sup>st</sup> -Order/Inviscid/TECNE <sup>(1)</sup>	-0.138	0.589
1 <sup>st</sup> -Order/Viscous/TECNE	-0.113	0.608
2 <sup>nd</sup> -Order/Inviscid/TECNE	-0.120	0.573
2 <sup>nd</sup> -Order/Viscous/TECNE	-0.103	0.575
1 <sup>st</sup> -Order/Inviscid/TCNE <sup>(2)</sup>	-0.139	0.588
1 <sup>st</sup> -Order/Viscous/TCNE	-0.114	0.605
2 <sup>nd</sup> -Order/Inviscid/TCNE	-0.119	0.570
2 <sup>nd</sup> -Order/Viscous/TCNE	-0.104	0.574

<sup>(1)</sup> TECNE: Thermal Equilibrium and Chemical Non-Equilibrium.

<sup>(2)</sup> TCNE: Thermal and Chemical Non-Equilibrium.

To the problem of the double ellipse, there is not a symmetric geometry in relation to the x axis. Hence, a different value of zero is expected to the lift coefficient. By Table 5, it is possible to note that the most severe value to  $c_L$  was that of the [16]

scheme with first-order accuracy, in an inviscid formulation, employing the thermochemical non-equilibrium model. The maximum  $c_D$  was obtained by the solution of the [16] scheme, first-order accurate, in a viscous formulation, employing the thermal equilibrium and chemical non-equilibrium model.

Table 6 exhibits the aerodynamic coefficients of lift and drag obtained by the problem of the reentry capsule, with structured discretization, to the reactive formulations. These coefficients are due to the pressure term alone. The contribution of the friction term was not considered.

To the problem of the reentry capsule, a symmetric geometry in relation to the x axis, a zero value is expected to the lift coefficient. By Table 6, it is possible to note that the solution closest to this value to  $c_L$  was that of the [16] scheme with first-order accuracy, in a viscous formulation, employing a thermochemical non-equilibrium model. The maximum  $c_D$  was obtained by the solution of the [16] scheme, first-order accurate, in a viscous formulation, employing a thermal equilibrium and chemical non-equilibrium model.

Table 6 Aerodynamic coefficients of lift and drag to the structured reentry capsule case.

Studied Case	$c_L$	$c_D$
1 <sup>st</sup> -Order/Inviscid/TECNE	$4.1 \times 10^{-10}$	3.99
1 <sup>st</sup> -Order/Viscous/TECNE	$-1.8 \times 10^{-10}$	4.38
2 <sup>nd</sup> -Order/Inviscid/TECNE	$2.6 \times 10^{-9}$	4.08
2 <sup>nd</sup> -Order/Viscous/TECNE	$-4.1 \times 10^{-10}$	4.31
1 <sup>st</sup> -Order/Inviscid/TCNE	$4.2 \times 10^{-10}$	3.98
1 <sup>st</sup> -Order/Viscous/TCNE	$-1.2 \times 10^{-10}$	4.37
2 <sup>nd</sup> -Order/Inviscid/TCNE	$2.4 \times 10^{-9}$	4.04
2 <sup>nd</sup> -Order/Viscous/TCNE	$-6.2 \times 10^{-10}$	4.30

#### 4.9 Quantitative Analysis

In terms of quantitative results, the present authors compared the reactive results with the perfect gas solutions. The stagnation pressure at the double ellipse and the reentry capsule noses was evaluated assuming the perfect gas formulation. Such parameter calculated at this way is not the best comparisons, but in the absence of practical reactive results, these constitute the best available results.

To calculate the stagnation pressure ahead of the double ellipse, [31] presents in its B Appendix values of the normal shock wave properties ahead of the configurations. The ratio  $pr_0/pr_\infty$  is estimated as function of the normal Mach number and the stagnation pressure  $pr_0$  can be determined from this parameter. Hence, to a freestream Mach number of

15.0, the ratio  $pr_0/pr_\infty$  assumes the value 290.20. The value of  $pr_\infty$  is determined by the following expression:

$$pr_\infty = \frac{pr_{\text{initial}}}{\rho_\infty \times a_\infty^2} \quad (20)$$

In the present study, for the double ellipse case,  $pr_{\text{initial}} = 794 \text{ N/m}^2$ ,  $\rho_\infty = 0.001 \text{ kg/m}^3$  and  $a_\infty = 334.210 \text{ m/s}$ . Considering these values, one concludes that  $pr_\infty = 7.109$  (non-dimensional). Using the ratio obtained from [31], the stagnation pressure ahead of the configuration nose is estimated as 2,063.03 unities. Table 7 compares the values obtained from the simulations with this theoretical parameter and presents the numerical percentage errors. As can be observed, all solutions present percentage errors less than 22.00%, which is a reasonable estimation of the stagnation pressure.

**Table 7 Comparisons between theoretical and numerical results (Double Ellipse).**

Case	$pr_0$	Error (%)
Inviscid/Structured/1 <sup>st</sup> Order	1,628.59	21.06
Viscous/Structured/1 <sup>st</sup> Order	1,859.08	9.89
Inviscid/Structured/2 <sup>nd</sup> Order	1,723.96	16.44
Viscous/Structured/2 <sup>nd</sup> Order	1,836.43	10.98
Inviscid/Unstructured/1 <sup>st</sup> Order	1,731.01	16.09
Viscous/Unstructured/1 <sup>st</sup> Order	1,881.12	8.82

The same analysis is valid to the reentry capsule problem. In the present study, for the reentry capsule case,  $pr_{\text{initial}} = 3,885 \text{ N/m}^2$ ,  $\rho_\infty = 0.004 \text{ kg/m}^3$  and  $a_\infty = 317.024 \text{ m/s}$ . Considering these values, one concludes that  $pr_\infty = 9.664$  (non-dimensional). Using the ratio obtained from [31], the stagnation pressure ahead of the configuration nose is estimated as 1,405.73 unities. Table 8 compares the values obtained from the simulations with this theoretical parameter and presents the numerical percentage errors. As can be observed, all solutions present percentage errors less than 10.00%, which is a good estimation of the stagnation pressure.

**Table 8 Comparisons between theoretical and numerical results (Reentry Capsule).**

Case	$pr_0$	Error (%)
Inviscid/Structured/1 <sup>st</sup> Order	1,296.75	7.75
Viscous/Structured/1 <sup>st</sup> Order	1,387.52	1.30
Inviscid/Structured/2 <sup>nd</sup> Order	1,311.97	6.67
Viscous/Structured/2 <sup>nd</sup> Order	1,351.02	3.89

#### 4.10 Computational Performance of the Studied Algorithms

Table 9 presents the computational data of the reactive simulations performed with the [16] scheme to the problem of the double ellipse in two-dimensions. In this table are exhibited the studied case, the maximum number of CFL employed in the simulation and the number of iterations to convergence. The maximum numbers of CFL presented the following distribution: 0.3 in four (4) cases (33.33%), 0.2 in six (6) cases (50.00%) and 0.1 in two (2) cases (16.67%). The convergence iterations did not overtake 7,000, in all studied cases. However, the time wasted in the simulations was much raised, taking until days (2) to convergence (to four orders of reduction in the maximum residual and viscous cases). This aspect can be verified in the computational costs presented in Tab. 11.

**Table 9 Computational data of the reactive simulations to the double ellipse.**

Studies case:	CFL:	Iterations:
1 <sup>st</sup> -Order/S <sup>(1)</sup> /I <sup>(2)</sup> /2D/TECNE	0.3	851
1 <sup>st</sup> -Order/S/V <sup>(3)</sup> /2D/TECNE	0.3	2,041
2 <sup>nd</sup> -Order/S/I/2D/TECNE	0.3	711
2 <sup>nd</sup> -Order/S/V/2D/TECNE	0.3	2,397
1 <sup>st</sup> -Order/U <sup>(4)</sup> /I/2D/TECNE	0.2	2,221
1 <sup>st</sup> -Order/U/V/2D/TECNE	0.1	6,570
1 <sup>st</sup> -Order/S/I/2D/TCNE	0.2	1,219
1 <sup>st</sup> -Order/S/V/2D/TCNE	0.2	3,013
2 <sup>nd</sup> -Order/S/I/2D/TCNE	0.2	1,018
2 <sup>nd</sup> -Order/S/V/2D/TCNE	0.2	2,734
1 <sup>st</sup> -Order/U/I/2D/TCNE	0.2	2,205
1 <sup>st</sup> -Order/U/V/2D/TCNE	0.1	6,407

<sup>(1)</sup> S: Structured; (2) I: Inviscid; (3) V: Viscous; (4) U: Unstructured.

**Table 10 Computational data of the reactive simulations to the reentry capsule.**

Studies case:	CFL:	Iterations:
1 <sup>st</sup> -Order/S/I/2D/TECNE	0.4	1,050
1 <sup>st</sup> -Order/S/V/2D/TECNE	0.1	7,805
2 <sup>nd</sup> -Order/S/I/2D/TECNE	0.4	880 (3) <sup>(1)</sup>
2 <sup>nd</sup> -Order/S/V/2D/TECNE	0.1	4,879 (3)
1 <sup>st</sup> -Order/S/I/2D/TCNE	0.4	1,136
1 <sup>st</sup> -Order/S/V/2D/TCNE	0.1	6,882
2 <sup>nd</sup> -Order/S/I/2D/TCNE	0.4	780 (3)
2 <sup>nd</sup> -Order/S/V/2D/TCNE	0.1	3,941 (3)

<sup>(1)</sup>: Orders of reduction of the residual magnitude.

Table 10 presents the computational data of the reactive simulations performed with the [16] scheme to the problem of the reentry capsule in two-dimensions. In this table are exhibited the studied case, the maximum number of CFL employed in the simulation and the number of iterations to convergence. The maximum numbers of CFL presented the following distribution: 0.4 in four (4) cases (50.00%), and 0.1 in four (4) cases (50.00%). The convergence iterations did not overtake 8,000, in all studied cases. However, the time wasted in the simulations was much raised, taking until days (3) to convergence (to four orders of reduction in the maximum residual and viscous cases). This aspect can be verified in the computational costs presented in Tab. 11.

It is important to emphasize that all two-dimensional viscous simulations were considered laminar, without the introduction of a turbulence model, although high Reynolds number were employed in the simulations.

Table 11 exhibits the computational costs of the [16] scheme in the two-dimensional reactive formulations. This cost is evaluated in seconds/per iteration/per computational cell. They were calculated using a notebook with processor INTEL PENTIUM Dual Core with 2.3GHz of "clock" and 2.0 GBytes of RAM, in the Windows 7 environment. In the two-dimensional case, considering thermal equilibrium and chemical non-equilibrium, the cheapest algorithm was due to [16], inviscid, first-order of accuracy, unstructured, whereas the most expensive was due to [16], viscous, second-order accurate, structured. In terms of the relative percentage error, the former is 55.01% cheaper than the later. Considering, now, thermochemical non-equilibrium, the cheapest algorithm was due to [16], inviscid, first-order of accuracy, unstructured, whereas the most expensive was due to [16], viscous, second-order accurate, structured. In terms of relative percentage error, the former is 59.64%

cheaper than the later. The computational costs due to a thermochemical non-equilibrium model are, in general, more expensive than the thermal equilibrium and chemical non-equilibrium ones.

**Table 11. Computational costs of the [16] scheme in the reactive cases.**

Studied Case	Computational Cost <sup>(1)</sup>
I/1 <sup>st</sup> -Order/S/2D/TECNE	0.000684
V/1 <sup>st</sup> -Order/S/2D/TECNE	0.001075
I/2 <sup>nd</sup> -Order/S/2D/TECNE	0.001013
V/2 <sup>nd</sup> -Order/S/2D/TECNE	0.001438
I/1 <sup>st</sup> -Order/U/2D/TECNE	0.000647
V/1 <sup>st</sup> -Order/U/2D/TECNE	0.000775
I/1 <sup>st</sup> -Order/S/2D/TCNE	0.001554
V/1 <sup>st</sup> -Order/S/2D/TCNE	0.002086
I/2 <sup>nd</sup> -Order/S/2D/TCNE	0.003132
V/2 <sup>nd</sup> -Order/S/2D/TCNE	0.003305
I/1 <sup>st</sup> -Order/U/2D/TCNE	0.001334
V/1 <sup>st</sup> -Order/U/2D/TCNE	0.002552

<sup>(1)</sup> Measured in seconds/per iteration/per computational cell.

## 5 Conclusions

This work, the second part of this study, presents a numerical tool implemented to simulate inviscid and viscous flows employing the reactive gas formulation of thermochemical non-equilibrium flow in two-dimensions. The Euler and Navier-Stokes equations, employing a finite volume formulation, on the context of structured and unstructured spatial discretizations, are solved. These variants allow an effective comparison between the two types of spatial discretization aiming verify their potentialities: solution quality, convergence speed, computational cost, etc. The aerospace problems involving the "hot gas" hypersonic flow around a double ellipse and around a reentry capsule, in two-dimensions, are simulated.

To the simulations with unstructured spatial discretization, a structured mesh generator developed by the first author ([32]), which creates meshes of quadrilaterals (2D), was employed. After that, as a pre-processing stage ([33]), such meshes were transformed in meshes of triangles. Such procedure aimed to avoid the time which would be waste with the implementation of an unstructured generator, which was not the objective of the present work, and to obtain a generalized algorithm to the solution of the reactive equations.

In this work, the unstructured formulation of the two-dimensional Euler and Navier-Stokes reactive

equations is presented. In [20], the first part of this study, it was presented the structured version of the calculation algorithm in two-dimensions. This work completes the formulation on structured and on unstructured contexts. However, solutions to the structured and unstructured cases are presented in both papers.

The reactive simulations involved an air chemical model of five species: N, O, N<sub>2</sub>, O<sub>2</sub> and NO. Seventeen chemical reactions, involving dissociation and recombination, were simulated by the proposed model. The Arrhenius formula was employed to determine the reaction rates and the law of mass action was used to determine the source terms of each gas species equation.

The algorithm employed to solve the reactive equations was the [16], first- and second-order accurate. The second-order numerical scheme was obtained by a "MUSCL" extrapolation process in the structured case (details in [17] and [35]). This process gives to the [16] algorithm TVD properties, which enhances its solutions quality. For more details about TVD algorithms in 2D and 3D, the reader is encouraged to read [36-39]. In the unstructured case, only first order solutions are presented. The algorithm was implemented in a FORTRAN programming language, using the software Microsoft Visual Studio 2008. Simulations with a notebook with processor INTEL PENTIUM Dual Core 2.30GHz of "clock" and 2.0GBytes of RAM memory was employed to perform the numerical experiments.

The results have demonstrated that the most correct aerodynamic coefficient of lift is obtained by the [16] scheme with second-order accuracy, in a viscous formulation, to a reactive condition of thermochemical non-equilibrium. Considering thermochemical non-equilibrium, the cheapest algorithm was due to [16], inviscid, first-order accurate, unstructured. Moreover, the shock position is closer to the geometry as using the reactive formulation than the ideal gas formulation. It was verified in the inviscid and viscous cases. In comparison with the perfect gas formulation, the reactive simulations gave the best results to the [16] scheme in its second order accuracy version, according to the expected behaviour for a high resolution scheme. Errors less than 22% were obtained with this version of the [16] algorithm in the determination of the stagnation pressure at the body nose, for both double ellipse and reentry capsule configurations, emphasizing the correct implementation and good results obtained from the reactive formulation. Values of this parameter were

evaluated and proved the significant potential of the present numerical tool.

## 6 Acknowledgments

The first author acknowledges the CNPq by the financial support conceded under the form of a DTI (Industrial Technological Development) scholarship no. 384681/2011-5. He also acknowledges the infrastructure of the ITA that allowed the realization of this work.

### References:

- [1] P. A. Gnoffo, R. N. Gupta, J. L. Shinn, Conservation Equations and Physical Models for Hypersonic Flows in Thermal and Chemical Nonequilibrium, *NASA TP 2867*, 1989.
- [2] J. H. Lee, Basic Governing Equations for the Flight Regimes of Aeroassisted Orbital Transfer Vehicles, Thermal Design of Aeroassisted Transfer Vehicles, *Progress in Astronautics and Aeronautics*, AIAA, Vol. 96, 1985, pp. 3-53.
- [3] R. N. Gupta, J. M. Yos, R. A. Thompson, K. -P. Lee, A Review of Reaction Rates and Thermodynamic and Transport Properties for an 11-Species Air Model for Chemical and Thermal Nonequilibrium Calculations to 30000 K, *NASA, RP-1232*, 1990.
- [4] R. K. Prabhu, An Implementation of a Chemical and Thermal Nonequilibrium Flow Solver on Unstructured Meshes and Application to Blunt Bodies, *NASA, CR 194967*, 1994.
- [5] C. Park, Radiation Enhancement by Nonequilibrium in Earth's Atmosphere, *Journal of Spacecraft and Rockets*, Vol. 22, No. 1, 1985, pp. 27-36.
- [6] C. Park, Problem of Rate Chemistry in the Flight Regimes of Aeroassisted Orbital Transfer Vehicles, Thermal Design of Aeroassisted Orbital Transfer Vehicles: *Progress in Astronautics and Aeronautics*, edited by H. F. Nelson, AIAA, NY, Vol. 96, 1985, pp. 511-537.
- [7] P. A. Gnoffo, Three-Dimensional AOTV Flowfields in Chemical Nonequilibrium, *AIAA Paper 86-0230*, 1986.
- [8] C. P. Li, Implicit Methods for Computing Chemically Reacting Flow, *NASA, TM 58274*, 1986.
- [9] C. Park, Convergence of Computation of Chemically Reacting Flows, Thermophysical Aspects of Re-entry Flows: *Progress in*

- Astronautics and Aeronautics*, edited by J. N. Moss and C. D. Scott, AIAA, NY, Vol. 103, 1986, pp. 478-513.
- [10] C. Park, Assessment of Two-Temperature Kinetic Model for Dissociating and Weakly-Ionizing Nitrogen. *AIAA, Paper 86-1347*, 1986.
- [11] C. Park, Calculation of Nonequilibrium Radiation in the Flight Regimes of Aeroassisted Orbital Transfer Vehicles, Thermal Design of Aeroassisted Orbital Transfer Vehicles: *Progress in Astronautics and Aeronautics*, edited by H. F. Nelson, AIAA, NY, Vol. 96, 1985, pp. 395-418.
- [12] C. Park, Nonequilibrium Air Radiation (NEQAIR) Program: User's Manual, *NASA, TM 86707*, 1985.
- [13] R. A. Allen, J. C. Camm, and J. C. Keck, Radiation from Hot Nitrogen, Research Report 102, *AVCO-Everett Research Laboratory*, Everett, MA, 1961.
- [14] R. A. Allen, J. C. Keck, J. C. Camm, Nonequilibrium Radiation from Shock Heated Nitrogen and a Determination of the Recombination Rate, Research Report 110, *AVCO-Everett Research Laboratory*, Everett, MA, 1961.
- [15] R. A. Allen, Nonequilibrium Shock Front Rotational, Vibrational, and Electronic Temperature Measurements. Research Report 186, *AVCO-Everett Research Laboratory*, Everett, MA, 1964.
- [16] B. Van Leer, Flux-Vector Splitting for the Euler Equations, *Lecture Notes in Physics*. Springer Verlag, Berlin, Vol. 170, 1982, pp. 507-512.
- [17] C. Hirsch, *Numerical Computation of Internal and External Flows – Computational Methods for Inviscid and Viscous Flows*, John Wiley & Sons Ltd, 691p, 1990.
- [18] E. S. G. Maciel, Analysis of Convergence Acceleration Techniques Used in Unstructured Algorithms in the Solution of Aeronautical Problems – Part I, *Proceedings of the XVIII International Congress of Mechanical Engineering (XVIII COBEM)*, Ouro Preto, MG, Brazil, 2005. [CD-ROM]
- [19] E. S. G. Maciel, Analysis of Convergence Acceleration Techniques Used in Unstructured Algorithms in the Solution of Aerospace Problems – Part II, *Proceedings of the XII Brazilian Congress of Thermal Engineering and Sciences (XII ENCIT)*, Belo Horizonte, MG, Brazil, 2008. [CD-ROM]
- [20] E. S. G. Maciel and A. P. Pimenta, Thermochemical Non-Equilibrium Reentry Flows in Two-Dimensions – Part I, *WSEAS Transactions on Mathematics*, Vol. 11, June, Issue 6, 2012, pp. 520-545.
- [21] S. K. Saxena and M. T. Nair, An Improved Roe Scheme for Real Gas Flow, *AIAA Paper 2005-587*, 2005.
- [22] E. S. G. Maciel, Relatório ao CNPq (Conselho Nacional de Desenvolvimento Científico e Tecnológico) sobre as atividades de pesquisa realizadas no período de 01/07/2008 até 30/06/2009 com relação ao projeto PDJ número 150143/2008-7, Report, *National Council of Scientific and Technological Development (CNPq)*, São José dos Campos, SP, Brazil, 102p, 2009. [available in the website [www.edissonsavio.eng.br](http://www.edissonsavio.eng.br)]
- [23] E. S. G. Maciel and A. P. Pimenta, Reentry Flows in Chemical Non-Equilibrium in Two-Dimensions, *Proceedings of the 10th International Symposium on Combustion and Energy Utilisation (ICCEU 2010)*, Mugla, Turkey, 2010.
- [24] C. Park, Assessment of Two-Temperature Kinetic Model for Ionizing Air, *Journal of Thermophysics and Heat Transfer*, Vol. 3, No. 13, 1989, pp. 233-244.
- [25] D. Ait-Ali-Yahia, W. G. Habashi, Finite Element Adaptive Method for Hypersonic Thermochemical Nonequilibrium Flows, *AIAA Journal*, Vol. 35, No. 8, 1997, pp. 1294-1302.
- [26] E. S. G. Maciel, Relatório ao CNPq (Conselho Nacional de Desenvolvimento Científico e Tecnológico) sobre as atividades de pesquisa realizadas no período de 01/07/2009 até 31/12/2009 com relação ao projeto PDJ número 150143/2008-7, Report, *National Council of Scientific and Technological Development (CNPq)* São José dos Campos, SP, Brazil, 102p, 2009. [available in the website [www.edissonsavio.eng.br](http://www.edissonsavio.eng.br)]
- [27] L. Landau and E. Teller, Theory of Sound Dispersion, *Physikalische Zeitschrift Der Sowjetunion*, Vol. 10, 1936, pp. 34-43.
- [28] L. N. Long, M. M. S. Khan, H. T. Sharp, Massively Parallel Three-Dimensional Euler / Navier-Stokes Method, *AIAA Journal*, Vol. 29, No. 5, 1991, pp. 657-666.
- [29] R. W. Fox, A. T. McDon-ald, *Introdução à Mecânica dos Fluidos*, Guanabara Editor, 1988.
- [30] E. S. G. Maciel, Relatório ao CNPq (Conselho Nacional de Desenvolvimento Científico e Tecnológico) sobre as atividades de pesquisa realizadas no período de 01/10/2011 até 30/09/2012 com relação ao projeto DTI-1, número 384681/2011-5, Report *National*

*Council of Scientific and Technological Development (CNPq)*, São José dos Campos, SP, Brazil, 50p, 2012. [available in the website [www.edissonsavio.eng.br](http://www.edissonsavio.eng.br)]

- [31] J. D. Anderson Jr., *Fundamentals of Aerodynamics*, McGraw-Hill, Inc., 5<sup>th</sup> Edition, 2010.
- [32] E. S. G. Maciel, Relatório ao Conselho Nacional de Pesquisa e Desenvolvimento Tecnológico (CNPq) sobre as Atividades de Pesquisa Desenvolvidas no Primeiro Ano de Vigência da Bolsa de Estudos para Nível DCR-IF Referente ao Processo No. 304318/2003-5, Report, *National Council of Scientific and Technological Development (CNPq)*, Recife, PE, Brazil, 37p, 2004. [available in the website [www.edissonsavio.eng.br](http://www.edissonsavio.eng.br)]
- [33] E. S. G. Maciel, Relatório ao Conselho Nacional de Pesquisa e Desenvolvimento Tecnológico (CNPq) sobre as Atividades de Pesquisa Desenvolvidas no Segundo Ano de Vigência da Bolsa de Estudos para Nível DCR-IF Referente ao Processo No. 304318/2003-5, Report, *National Council of Scientific and Technological Development (CNPq)*, Recife, PE, Brazil, 54p, 2005. [available in the website [www.edissonsavio.eng.br](http://www.edissonsavio.eng.br)]
- [34] E. S. G., Maciel, and Pimenta, A. P., Chemical Non-Equilibrium Reentry Flows in Two-Dimensions – Part I, Submitted to *WSEAS Transactions on Applied and Theoretical Mechanics*, 2012 (under review).
- [35] E. S. G., Maciel, Explicit and Implicit TVD High Resolution Schemes in 2D, *Transactions on Applied and Theoretical Mechanics*, Vol. 7, April, Issue 3, 2012, pp. 182--209.
- [36] E. S. G., Maciel, Solutions of the Euler and the Laminar and Turbulent Navier-Stokes Equations in Two-Dimensions Using TVD and ENO Algorithms, *WSEAS Transactions on Mathematics*, Vol. 11, June, Issue 6, 2012, pp. 478-500.
- [37] E. S. G., Maciel, TVD Algorithms Applied to the Solution of the Euler and Navier-Stokes Equations in Three-Dimensions, *WSEAS Transactions on Mathematics*, Vol. 11, June, Issue 6, 2012, pp. 546-572.
- [38] E. S. G., Maciel, TVD Flux Vector Splitting Algorithms Applied to the Solution of the Euler and Navier-Stokes Equations in Three-Dimensions – Part I, *WSEAS Transactions on Applied and Theoretical Mechanics*, Vol. 7, April, Issue 2, 2012, pp. 112-139.
- [39] E. S. G., Maciel, TVD Flux Vector Splitting Algorithms Applied to the Solution of the Euler

and Navier-Stokes Equations in Three-Dimensions – Part II, *WSEAS Transactions on Applied and Theoretical Mechanics*, Vol. 7, April, Issue 2, 2012, pp. 140-158.